

Manipulating the electronic polarization in a magnetoelectric antiferromagnet via the two-photon Stark effect

Xinshu Zhang,¹ Tyler Carbin,¹ Adrian B. Culver,^{1,2} Kai Du,³ Kefeng Wang,³ Sang-Wook Cheong,³ Rahul Roy,^{1,2} and Anshul Kogar^{1,*}

¹*Department of Physics and Astronomy, University of California Los Angeles, Los Angeles, CA 90095, USA*

²*Mani L. Bhaumik Institute for Theoretical Physics, Department of Physics and Astronomy, University of California Los Angeles, Los Angeles, CA 90095, USA*

³*Rutgers Center for Emergent Materials, Rutgers University, Piscataway, NJ, USA*

(Dated: July 25, 2023)

When intense light is shone through a transparent medium, the strong, time-periodic potential from the radiation field reshapes the many-body Hamiltonian. Crucially, this interaction does not involve light absorption and, in principle, does not generate any heat. The incident radiation can nonetheless be used to optically tailor various degrees of freedom, leading to the possibility of photo-controlling macroscopic properties of matter. Here, we show that when inversion symmetry is broken by the antiferromagnetic spin arrangement in Cr_2O_3 , transmitting linearly polarized light through the crystal gives rise to a purely electronic dipole moment by way of a two-photon Stark effect. Using interferometric time-resolved second harmonic generation, we show that the threefold rotational symmetry of the crystal is broken only while the pump pulse is present; the timescale indicates that an electronic response is generated without affecting the magnetic or crystal structures. The orientation of the induced moment depends on the incident light polarization, which allows for contact-free control of the dipole moment vector. Our results establish a dissipationless optical protocol by which to selectively polarize the electronic subsystem and provides a method to manipulate electronic symmetries in noncentrosymmetric insulators.

The macroscopic electric polarization, \mathbf{P} , is the most fundamental quantity that describes dielectric media. For \mathbf{P} to be finite in crystalline solids, the medium must lack an inversion center, more than one rotation axis, and an improper rotation axis. These symmetry requirements can be met by the application of an appropriate external field or through the spontaneous breaking of symmetries across a phase transition [1, 2]. Two contributions determine the electric polarization – the ionic and the electronic subsystems [3, 4]. Experimentally, it is extremely difficult to isolate either component. However, this separation is essential to understanding the driving mechanisms behind the ferroelectric and magnetoelectric effects in correlated materials, where the electronic subsystem is thought to play a major role [5–10].

One method to isolate the electronic subsystem is to

use a “Floquet engineering” protocol [11–13]. In this approach, an ultrashort light pulse is shone below the electronic gap to avoid absorption; the electrons can then be driven coherently by the light’s oscillating electric field. So far, this concept has led to the manipulation of spin dynamics in magnets and to the engineering of energy level shifts in semiconductors. To selectively address the spins, light is used to magnetize the system through the inverse Faraday effect or the inverse Cotton-Moutton effect [14, 15]. On the other hand, energy levels shifts can be induced through the AC Stark and/or Bloch-Siegert effects which give rise to a light-assisted level repulsion [16–20]. While these cases exemplify dynamical control of magnetic and spectral properties of matter, similar sub-gap optical manipulation of the electronic polarization has yet to be definitively demonstrated [21, 22]. It has long been known, however, that in systems lacking inversion symmetry, a strong periodic drive can induce a finite quasi-DC polarization [23].

In this work, we show that, by shining light in the transparency window of a noncentrosymmetric but non-polar antiferromagnet, optical rectification can be used to selectively and controllably polarize the electronic subsystem through a two-photon Stark effect. Optical rectification is a nonlinear process whereby light’s oscillating electric field generates a quasi-DC electric polarization [24]. To leading order, the induced polarization is:

$$\mathbf{P}(\omega_0) = \chi_{OR}^e(\omega_0; \omega_1, -\omega_2) \mathbf{E}(\omega_1) \mathbf{E}(-\omega_2), \quad (1)$$

where $\mathbf{E}(\omega_j)$ ($j=1, 2$) is the electric field vector of the incident light, $\chi_{OR}^e(\omega_0; \omega_1, -\omega_2)$ is the second-order nonlinear susceptibility tensor that describes optical rectification, and the frequency of the rectified response is given by $\omega_0 = \omega_1 - \omega_2$ with $\omega_1 \approx \omega_2$. When light pulses shorter than the typical structural response timescales are used to generate a rectified field, one could, in principle, distinguish between a structural and an electronic polarization based on the system’s relaxation dynamics.

To observe the induced dipole moment, we probe the system with rotational anisotropy second harmonic generation (RA-SHG), a technique sensitive to electronic symmetries [25–27]. In our experimental configuration,

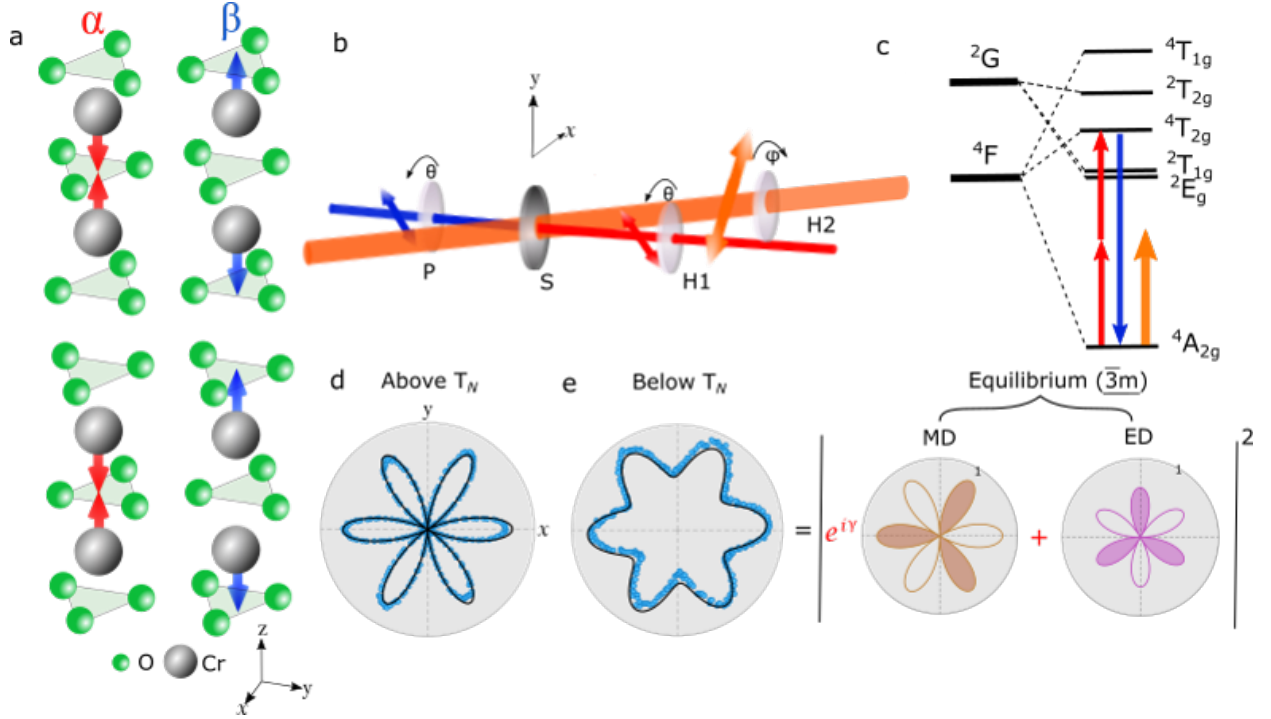


FIG. 1: (a) Crystal structure and spin arrangement below T_N in Cr_2O_3 . Two antiferromagnetic (AFM) domains are possible, which we label α (red) and β (blue), where arrows represent the spins on the Cr site. (b) Illustration of our time-resolved second harmonic generation (SHG) experimental setup. H1 is the half wave plate and P is the polarizer to select the polarization of the incident fundamental and output second harmonic light, respectively. The H1 and P rotate together such that the input and output polarization are synchronized at angle θ relative to y -axis. H2 is the half wave plate used to adjust angle of the polarization, φ , of the pump light relative to the y -axis. S denotes the sample. (c) Schematic energy levels of Cr_2O_3 split by the crystal effective field (CEF). The second harmonic generation process is depicted with the two red arrows (incident photons) and the blue arrow (second harmonic photon). The pump energy is below all the CEF excitations (orange arrow). (d) Equilibrium rotational anisotropy second harmonic generation (RA-SHG) patterns for the β AFM domain above and (e) below T_N , at 310 K and 150 K, respectively. Below T_N , there are two contributions to the second harmonic signal coming from magnetic dipole radiation (brown) and electric dipole radiation (purple). The shaded regions are contrasted to the transparent regions to indicate where the SHG amplitude changes sign. The magnitudes are normalized to 1.

both the incident fundamental and detected second harmonic light beams are polarized along the same direction (Fig. 1(b)). As a model compound, we select the prototypical linear magnetoelectric Cr_2O_3 [28–42]. Above $T_N \approx 307$ K, Cr_2O_3 crystallizes in the point group $\bar{3}m$ (D_{3d}) in which electric dipole SHG is forbidden due to the presence of inversion symmetry; however, when the second harmonic energy is tuned to a Cr d - d electronic transition ($^4A_{2g}(t_{2g})^3 \rightarrow ^4T_{2g}(t_{2g})^2e_g$) at 2.1 eV (590 nm), resonant magnetic dipole SHG is observed (Fig. 1(c)-(d)) [30]. As shown in Fig. 1(d), the RA-SHG pattern is consistent with the threefold symmetry of the crystal when the probe light propagates along the out-of-plane direction (and is polarized in-plane). The RA-SHG pattern can be fit with a magnetic dipole source term of the following form (black line in Fig. 1(d)):

$$I(2\omega; T > T_N) \propto |\chi^m \sin(3\theta)|^2 \quad (2)$$

which contains a single fit parameter, χ^m , the in-plane magnetic dipole second harmonic susceptibility. Here, ω

is the frequency of the probe light and θ represents the angle of the incident and detected light polarization with respect to the sample's y -axis (Fig. 1 (b)).

Below T_N , Cr_2O_3 orders antiferromagnetically with the four Cr spins in the unit cell alternating in an up and down sequence along the rhombohedral optical axis (Fig. 1(a)). This spin structure breaks inversion symmetry, and the magnetic point group becomes $\bar{3}m$ [43]. Electric dipole SHG is then allowed (through the spin-orbit interaction) and interferes with the pre-existing magnetic dipole signal [29, 30]. Due to the interference between the magnetic and electric dipole signals, the nodes present in the RA-SHG pattern above T_N are lifted below T_N (Fig. 1(e)). That the nodes are lifted implies a phase difference between the magnetic and electric dipole SHG amplitudes at the probed wavelength. The RA-SHG pattern below T_N can be fit with a simple function that includes electric and magnetic dipole radiation, as shown in Fig. 1(e) [29, 30]:

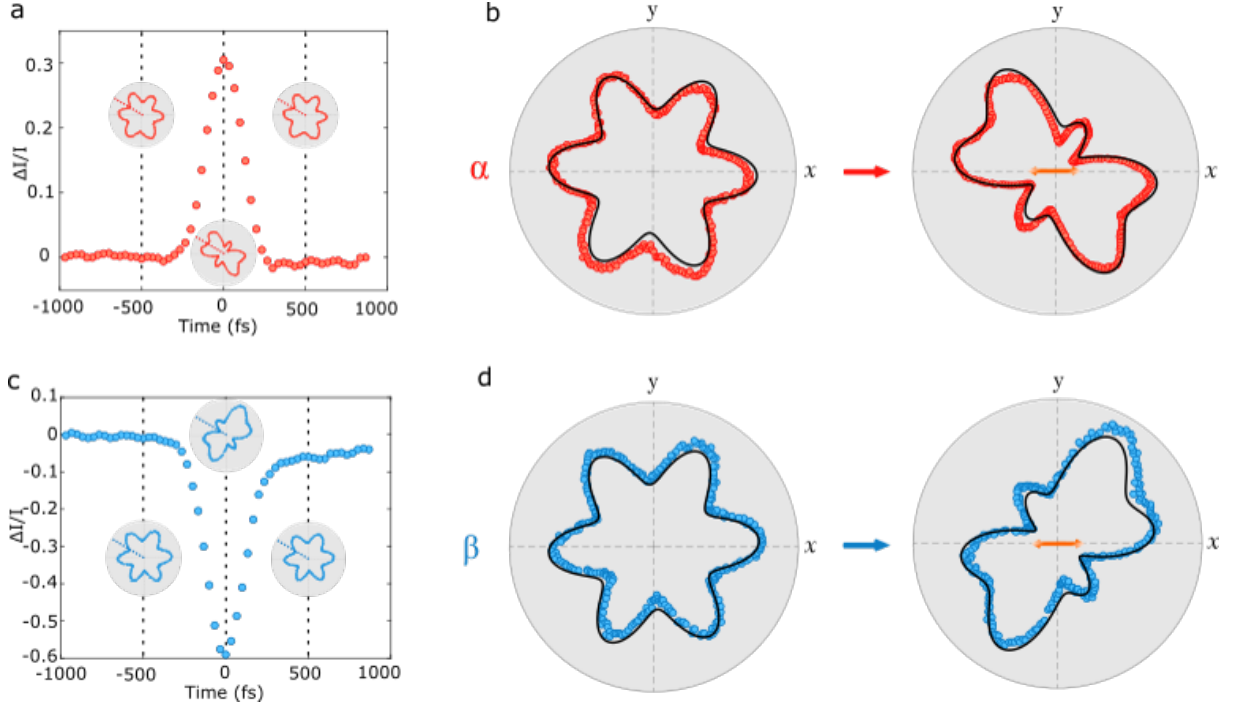


FIG. 2: (a) The normalized change to the SHG intensity at $T = 150$ K in the α domain as a function of time delay for pump light aligned along x -axis and probe fixed to $\theta \sim 60^\circ$. The fluence of the pump light is 20 mJ/cm^2 . Insets show three representative RA-SHG patterns at ± 500 fs and 0 fs. The red dashed line in RA-SHG pattern indicates the chosen direction of the probe polarization for the time scans. (b) Change in the RA-SHG pattern from possessing sixfold symmetry (left panel) to twofold symmetry (right panel) upon pumping the α domain. (c) Same as (a), but in the β domain. (d) Same as (b), but in the β domain. The solid black line in (d) is the fit using the function described in main text. Note that the black line in (b) is not a fit. It is obtained by flipping the sign of electric dipole contribution of the fit in (d) while keeping the magnetic dipole contribution fixed.

$$I(2\omega; T < T_N) \propto |e^{i\gamma} \chi^m \sin(3\theta) \pm \chi^e \cos(3\theta)|^2 \quad (3)$$

where the \pm depends on the AFM domain and γ denotes the relative phase between magnetic and electric dipole second harmonic radiation (see Supplementary Note I). Near but below T_N , the electric dipole SHG susceptibility, χ^e , is proportional to the antiferromagnetic (AFM) order parameter, \mathbf{L} . Thus, χ_e differs in sign between the two AFM domains, which we denote α and β (Fig. 1(a)) [30, 44]. In this equation, it is important to note that γ depends sensitively on the second harmonic energy (Supplementary Note VI). At the 2.1 eV second harmonic energy used here, $\gamma \approx 85^\circ$, and the two domains exhibit almost identical RA-SHG patterns (left panels of Fig. 2(b) and (d)).

We now move on to pump the Cr_2O_3 crystal with 1.2 eV (1030 nm) light pulses at a fluence of 20 mJ/cm^2 . The wavelength of the pump light lies in the transparency window of the crystal and away from electronic resonances to avoid significant absorption (orange arrow in Fig. 1(c)). As the linearly polarized pump light is transmitted through the crystal, we observe a drastic symmetry change in the RA-SHG pattern (right panels of

Fig. 2(b) and (d)). The RA-SHG pattern, which formerly respected the underlying threefold crystal symmetry, transiently exhibits only twofold symmetry. Additionally, the two domains, which are almost indistinguishable at equilibrium with RA-SHG, exhibit differing responses to the pump (the two domains are distinguishable at equilibrium with circularly polarized SHG [30]). With the SHG probe polarization fixed to $\theta = 60^\circ$, the second harmonic intensity decreases by about 60% in the β domain, while the intensity increases by 30% in the α domain (Fig. 2(a) and (c)). In these figures, the pump polarization is aligned along the x -axis, as indicated with the double-headed orange arrow in the right panels of Fig. 2(b) and (d). Notably, the symmetry reduction in the RA-SHG pattern is not observed above T_N or when the pump light is circularly polarized; instead the antiferromagnetism in addition to a well-defined polarization axis are both necessary to observe this symmetry breaking effect in Cr_2O_3 (Supplementary Notes III and V).

Importantly, we observe this effect only when the pump and probe pulses are temporally overlapped; the timescale characterizing this transient symmetry breaking is on the order of the laser pulse width (~ 200 fs) (Fig. 2(a) and (c)). (The slight asymmetry in the back-

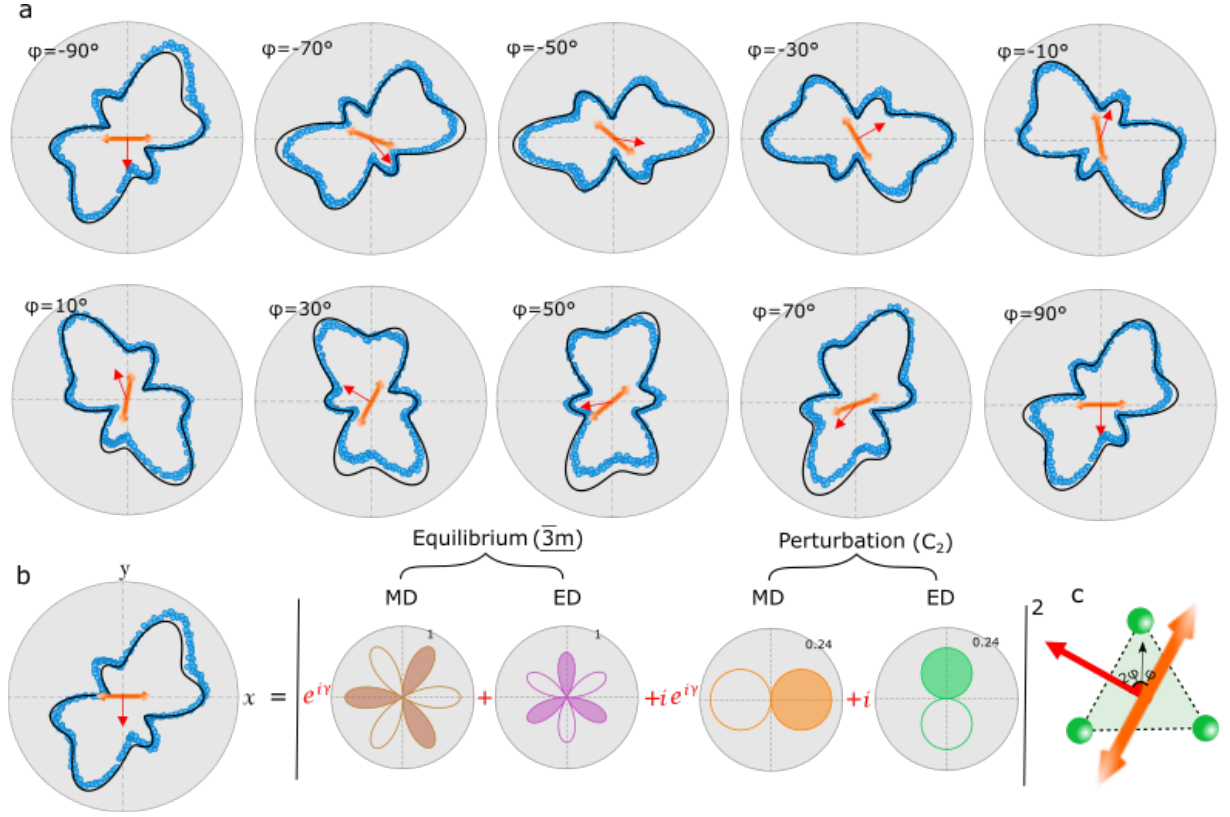


FIG. 3: (a) Evolution of RA-SHG pattern at $T = 150$ K in the β domain as the pump polarization is varied. Starting along x -axis, the polarization is rotated clockwise in 20° steps (orange double headed arrow). The pump polarization is defined with respect to y -axis. The orientation of the light-induced electronic dipole is shown with the red single-headed arrow. In these plots, only the pattern with $\varphi = -90^\circ$ is fit, while the rest of the black curves are obtained using Eq. 6 of the main text. (b) The four contributions to the RA-SHG pattern consist of the equilibrium magnetic and electric dipole radiation in addition to the pump-induced perturbations to the magnetic and electric dipole signals. These contributions are shown in brown, purple, orange and green. (c) A schematic showing the orientation of the electronic dipole (red) and the pump polarization (orange).

ground levels of the time traces is attributed to two-photon absorption and is unrelated to the symmetry-breaking.) In the insets of Fig. 2(a) and (c), we show RA-SHG patterns 500 fs before and after the pump pulse propagates through the probed region as well as the pattern when the pump and probe pulses are perfectly overlapped (the latter are also shown in the right panels of Fig. 2(b) and (d)). Noticeably, there is not a measurable relaxation timescale for the symmetry change, which suggests that neither the structural nor spin degrees of freedom bring about this reduction in symmetry. Instead, the electronic charge degree of freedom is solely involved.

To show that the origin of this transient symmetry breaking stems from an optically induced electronic dipole moment, we measure the dependence of the RA-SHG pattern on the pump polarization. Figure 3(a) reveals how the RA-SHG pattern in the β domain varies as the pump polarization is rotated clockwise in 20° steps. As the pump polarization angle, φ , is tuned, the shape and orientation of the RA-SHG pattern is correspondingly modified. However, every $\Delta\varphi = 60^\circ$, the shape of

the RA-SHG reappears but is rotated clockwise by the same amount due to the crystal symmetry. These observations indicate that the modification of the RA-SHG pattern is due to a vectorial perturbation which can be used to control the angle of the second harmonic emission. Based on symmetry arguments, we show below that the vectorial nature of the perturbation, coupled with the timescales involved and the differing SHG response from opposite AFM domains (Fig. 2), stems from a light induced polarization of the electronic subsystem.

Under this interpretation, the fits to the RA-SHG patterns are highly constrained. Mathematically, the electric/magnetic dipole susceptibility tensor describing SHG can be expanded to first order in the induced moment:

$$\chi_{SHG}^{e/m}(\mathbf{P}(\omega_0)) = \chi_{SHG}^{e/m}\big|_{\mathbf{P}=0} + \underbrace{\frac{\partial \chi_{SHG}^{e/m}}{\partial \mathbf{P}(\omega_0)}\bigg|_{\mathbf{P}=0}}_{\equiv \delta \chi_{SHG}^{e/m}} \mathbf{P}(\omega_0). \quad (4)$$

$\mathbf{P}(\omega_0)$ can be calculated based on the magnetic symmetry of the crystal and yields the following expression (see

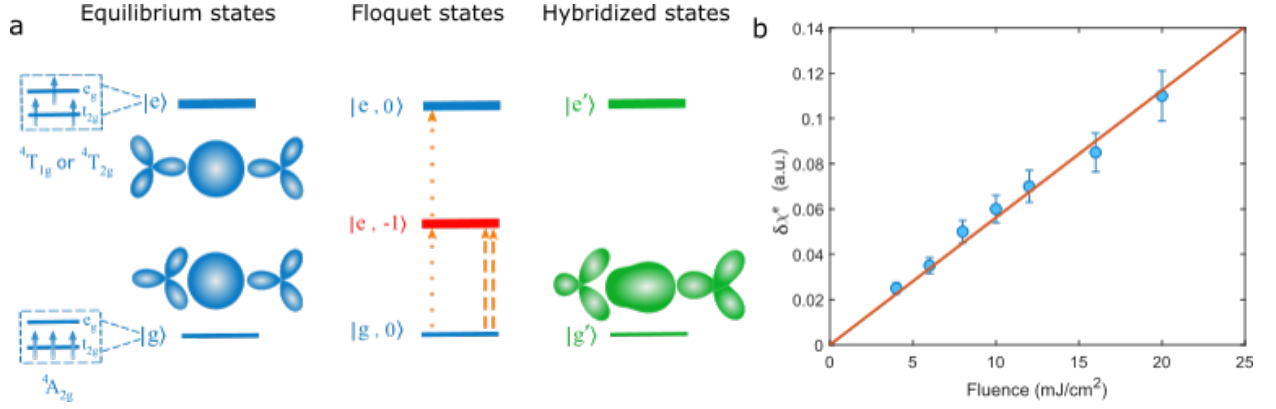


FIG. 4: (a) Energy levels and associated electronic probability densities demonstrating how the light-induced electric dipole arises via a two-photon Stark effect. At equilibrium, the ground state $|g\rangle$ (${}^4A_{2g}$) in Cr_2O_3 comprises three electrons in t_{2g} state. For illustration purposes, we draw the corresponding single electron probability densities in the $x-y$ plane (the symmetry of the states is discussed in Supplementary Note VII). The relevant excited state manifold $|e\rangle$ comprises both the ${}^4T_{2g}$ and ${}^4T_{1g}$ states, which consist of two t_{2g} electrons and one e_g electron. Representative electron probability densities are also shown. In the middle panel, we show that when applying the periodic drive, Floquet states $|e, -1\rangle$ are generated within the rotating wave approximation. There are two possible channels for generating a static electric dipole, which are indicated by the orange arrows. One path gives terms of the form $\langle g, 0 | \mathbf{d} | e, 0 \rangle$, while the other yields terms of the form $\langle e, -1 | \mathbf{d} | e, -1 \rangle$, where \mathbf{d} is the dipole operator. Both channels require a two-photon process. In the right panel, representative electron probability densities for the first dipole channel are shown, and a dipole can clearly be observed. (b) The fluence dependence of $\delta\chi^e$ (proportional to light-induced electric dipole, $\mathbf{P}(\omega_0)$) at $T = 150$ K. The linear dependence on fluence is consistent with a two-photon process.

Supplementary Note IIA):

$$\mathbf{P}(\omega_0) = \chi_{OR}^e I_{pump} (\sin(-2\varphi)\hat{\mathbf{x}} + \cos(-2\varphi)\hat{\mathbf{y}}), \quad (5)$$

where χ_{OR}^e is the in-plane susceptibility associated with optical rectification and I_{pump} is the intensity of the pump beam. By combining the generalized susceptibility tensor (Eq. 4) and the expression for the pump induced polarization (Eq. 5), we can derive the full expression for the SHG intensity as function of the pump polarization angle for the two domains (Supplementary Note IIB):

$$I(2\omega; \varphi) \propto |e^{i\gamma}\chi^m \sin(3\theta) \pm \chi^e \cos(3\theta) + ie^{i\gamma}\delta\chi^m \sin(\theta - 2\varphi) \pm i\delta\chi^e \cos(\theta - 2\varphi)|^2. \quad (6)$$

Compared to the equilibrium case, only two additional independent terms are permitted to model the RA-SHG pattern – perturbations to the in-plane electric and magnetic dipole susceptibilities, $\delta\chi^e$ and $\delta\chi^m$, respectively. In Fig. 3(b), we demonstrate that Eq. 6 yields an excellent fit to the RA-SHG pattern when the pump polarization is along x -axis (i.e. $\varphi = -90^\circ$).

Several non-trivial predictions of our fit model are consistent with our experimental observations and interpretation. First, below T_N , Cr_2O_3 loses an inversion center and an improper rotation axis. Only the presence of two separate rotation axes, one in-plane and one out-of-plane, forbids a finite polarization. The perturbation terms in Eq. 6 break the in-plane rotational symmetry of the crystal (Fig. 3(b)), which then permits a finite

dipole moment. Second, as the pump polarization angle, φ , is varied, the induced dipole moment is correspondingly rotated by an angle -2φ (Eq. 5 and 6). In Fig. 3(c), we illustrate this concept visually with the orange and red arrows which represent the orientations of the pump polarization and induced dipole moment, respectively. Once the RA-SHG pattern at $\varphi = -90^\circ$ is fit (Fig. 3(b)), the dependence on the pump polarization angle, φ , is completely determined by Eq. 6. The results generated using Eq. 6 are shown in the black curves of Fig. 3(a) and show good agreement with the data. We emphasize that these are not fits to the individual RA-SHG patterns; only the $\varphi = -90^\circ$ pattern is fit and the remaining black lines are generated by this function, where only a single parameter, φ , is varied. Third, the perturbation terms are 90° out of phase with respect to the corresponding unperturbed terms (i.e. there is a 90° phase difference between $\delta\chi^e$ and χ^e as well as between $\delta\chi^m$ and χ^m) which is accounted for by the coefficient i multiplying the perturbation terms in the fit model. This phase difference arises due to the \mathcal{PT} symmetry (parity, \mathcal{P} ; time-reversal, \mathcal{T}) in Cr_2O_3 (Supplemental Note IIC). Lastly, by choosing the opposite sign of χ^e and $\delta\chi^e$ in Eq. 6 (terms proportional to the order parameter near T_N), we obtain excellent agreement to the RA-SHG pattern of the opposite antiferromagnetic domain. Again, the black line in the right panel of Fig 2(b) is not a fit, but is generated from this procedure. Overall, our fit model is able to reproduce various experimentally observed aspects of the data and provides strong evidence in favor of an electronic dipole moment. However, the

model itself does not explain how the moment is generated microscopically.

To understand how the dipole is induced, we use a single-ion model of the Cr atoms in the crystal field environment. In Cr_2O_3 , the Cr atoms are surrounded by a trigonally-distorted oxygen octahedron. The Cr $3d^3$ electrons occupy the lower three t_{2g} states, which are split off from the higher e_g states by at least 2.1 eV (Fig. 4(a)). However, an electronic dipole moment cannot develop by considering only the Cr $3d$ subspace. A necessary (but not sufficient) condition for observing a dipole is the superposition of states with opposite parity. Above T_N , the trigonal distortion of the oxygen octahedron breaks inversion symmetry at the Cr site locally and therefore permits a superposition of the Cr $4p$ and $3d$ states. However, because global inversion symmetry is present in the crystal, both an equilibrium dipole moment and the optical rectification process are forbidden. Below T_N , in contrast, global inversion symmetry is broken by the magnetic structure, but an equilibrium dipole moment is still disallowed because Cr_2O_3 retains two rotational symmetry axes (threefold along the z - and twofold along the y -axis; Fig. 1(a)). A rectified response to a periodic drive, though, becomes possible.

To comprehend the effect of the drive, we appeal to the useful picture provided by Floquet theory. In the leftmost panel of Fig. 4(a), we schematically illustrate the energy levels in Cr_2O_3 and show examples of the corresponding in-plane probability densities. In this sketch, the ground state represents the ${}^4A_{2g}$ state while the excited states, $|e\rangle$, include all six ${}^4T_{2g}$ and ${}^4T_{1g}$ states. (For the purposes of this illustration, we are neglecting the splitting between the ${}^4T_{2g}$ and ${}^4T_{1g}$ which is roughly 0.6 eV). When a periodic potential is applied to the system, a series of Floquet sidebands or “dressed states” emerge, which we label $|j, n\rangle$, where j labels the equilibrium state from which the n^{th} Floquet sideband derives. In the middle panel of Fig. 4(a), we make the rotating wave approximation and only show the dressed states of the excited state manifold, $|e, -1\rangle$. Although this truncation works best when the drive is resonant between $|g\rangle$ and $|e\rangle$, this picture already provides a mechanism by which a static electronic dipole can be generated.

In this effectively time-independent scheme, a “hopping” is only possible between states separated by ± 1 in the Floquet index, where hopping matrix elements are given by terms like $\lambda \sim \langle j', n \pm 1 | \mathbf{d} \cdot \mathbf{E} | j, n \rangle$ [13]. Here, \mathbf{d} is the dipole operator and \mathbf{E} is the time-independent electric field vector, and therefore the value of the hopping matrix elements sensitively depends on the polarization of the incoming light. Schematically, a superposition state, $|g'\rangle = |g, 0\rangle + \lambda |e, -1\rangle + \lambda^2 |e, 0\rangle$, then forms due to this “hopping”, where the power of the coefficient λ indicates a first or second order perturbative correction to the ground state. The superposition between $|g, 0\rangle$ and $|e, 0\rangle$ must occur via the $|e, -1\rangle$ sideband, which is

why the coefficient scales with λ^2 . $|g'\rangle$ is capable of exhibiting a dipole moment (either oscillating at the laser frequency or static), which can be seen by calculating the expectation value $\langle g' | \mathbf{d} | g' \rangle$ (Supplementary Note VIII).

With the orange arrows in the middle panel of Fig. 4(a), we illustrate the two pathways through which a *static* dipole can develop. The first path is shown with the dotted arrows and indicates that a static dipole can arise due to terms of the form $\lambda^2 \langle g, 0 | \mathbf{d} | e, 0 \rangle \sim |\mathbf{E}|^2$. Selection rules associated with such matrix elements have been previously been calculated for Cr_2O_3 in Refs. [32–34]. We use the matrix elements therein to sketch representative probability densities for this kind of process in the rightmost panel of Fig. 4(a). Clearly, the in-plane threefold symmetry of the crystal is broken by this superposition and a dipole moment can be observed. In Supplementary Note VII, we discuss the symmetry of the t_{2g} and e_g states to clarify how these probability densities are sketched.

A second pathway, indicated with the dashed orange arrows, also gives rise to a static dipole moment. In this case, the expectation value of the dipole operator yields terms of the form $\lambda^2 \langle e, -1 | \mathbf{d} | e, -1 \rangle \sim |\mathbf{E}|^2$. Since the Floquet indices on either side of the matrix element are identical, the dipole moment is static. In both hopping pathways, non-vanishing dipole matrix elements among the excited state degenerate subspace is crucial for the observation of the static dipole. It is important to note that both pathways also give rise to terms that scale with $\lambda^2 \sim |\mathbf{E}|^2$. Such a relation implies that the lowest order static electric dipole moment scales with $|\mathbf{E}|^2$ (i.e. fluence), which is confirmed experimentally in Fig. 4(b). We thus refer to this electronic process as a two-photon Stark effect. Further details of the calculation using time-dependent perturbation theory and Floquet theory in addition to using the single-particle and multiparticle bases are presented in Supplementary Note VIII.

In conclusion, our experimental observations and simple theoretical account demonstrate how a purely electronic dipole moment develops in antiferromagnetic Cr_2O_3 via a two-photon Stark effect. By breaking in-plane rotational symmetry, light’s polarization is used to establish optical control of the dipole moment vector. Our experiment builds on previous work showing that purely electronic macroscopic effects in crystals can be induced with laser pulses using a “Floquet engineering” protocol. In principle, the generation of an electronic dipole moment in linear magnetoelectrics should produce a corresponding magnetic response; in compounds where the electronic component of the magnetoelectric effect is dominant, optical control of magnetism should be possible [11, 45–47]. Our work paves the way towards isolating and quantifying the electronic contribution of the magnetoelectric effect as well as the optical manipulation of magnetism through the magnetoelectric effect.

ACKNOWLEDGEMENTS:

We thank Mengxing Ye, Honglie Ning, Carina Belvin and Wesley Campbell for helpful conversations related to this work. Research at UCLA was supported by the U.S. Department of Energy (DOE), Office of Science, Office of Basic Energy Sciences under Award No. DE-SC0023017 (experiment and theory). The work at Rutgers was supported by W. M. Keck Foundation (materials synthesis).

AUTHOR CONTRIBUTIONS:

X.Z. and T.C. built the SHG setup and performed the time-resolved SHG experiments under the supervision of A.K. X.Z. analysed the data under the supervision of A.K. K.D. and K.W. grew the single crystals under the supervision of S.-W.C. Theoretical calculations were carried out by A.B.C. under the supervision of R.R. The manuscript was written by X.Z., A.B.C. and A.K. with input from all authors.

COMPETING INTERESTS:

The authors declare no competing interests.

METHODS

Sample synthesis

Cr_2O_3 single crystals were grown using a laser diode heated floating zone (LFZ) technique. Cr_2O_3 powders (Alfa Aesar, 99.99%) were pressed into 3 mm diameter rods under 8000 PSI hydrostatic pressure. The compressed rod was sintered at 1600°C in a box furnace for 10 hours. The crystals were grown with growth speed of 2 to 4 mm/h in oxygen flow of 0.1 l/min, and counter rotation of the feed and seed rods at 15 and 15 rpm, respectively.

Experimental details

The primary laser used in our experiment is based on a Yb:KGW gain medium that outputs a power of 10 W. The laser pulses have a Gaussian-like profile with an approximately 180 fs pulse duration and a 1030 nm central wavelength. In our experiment, we used a laser pulse repetition rate of 5 kHz. The fundamental output of the laser at 1030 nm was used as the pump pulse, which was focused obliquely on the sample at a 10 degree angle of incidence. The pump laser spot size was $\sim 500 \mu\text{m}$ and the maximum fluence was $\sim 20 \text{ mJ}/\text{cm}^2$. The probe pulse was generated from an optical parametric amplifier with tunable wavelength, which we use for the second harmonic spectroscopy between 900-1200 nm. The probe pulse was focused normally on the sample with a $100 \mu\text{m}$ spot size, and the probe fluence was $\sim 2 \text{ mJ}/\text{cm}^2$. Detection of the second harmonic light was conducted with a commercial photo-multiplier tube. The sample was cooled to 150 K with a standard optical cryostat with fused silica windows to prevent distortions to the light polarization.

DATA AVAILABILITY

The data that supports the findings of this study are present in the paper and/or in the supplementary information, and are deposited in the Zenodo repository. Additional data related to the paper is available from the corresponding authors upon reasonable request.

* Electronic address: anshulkogar@physics.ucla.edu

- [1] Powell, R. Symmetry, group theory, and the physical properties of crystals *Springer* (2010).
- [2] Landau, L. Electrodynamics of continuous media *elsevier* (2013).
- [3] Khomskii, D. Transition metal compounds *Cambridge University Press* (2014).
- [4] Bonfim, O. & Gehring, G. Magnetoelectric effect in anti-ferromagnetic crystals *Advances in Physics* **29**, 731-769 (1980).
- [5] Spaldin, N. & Ramesh, R. Advances in magnetoelectric multiferroics *Nat. Mater.* **18**, 203-212 (2019).
- [6] Spaldin, N. & Fiebig, M. The Renaissance of Magneto-electric Multiferroics *Science* **309**, 391-392 (2005).
- [7] Cheong, S. & Mostovoy, M. Multiferroics: a magnetic twist for ferroelectricity *Nat. Mater.* **6**, 13-20 (2007).
- [8] Khomskii, D. Transition metal compounds *Cambridge University Press* (2014).
- [9] Malashevich, A. et al. Full magnetoelectric response of Cr_2O_3 from first principles *Phys. Rev. B* **86**, 094430 (2012).
- [10] Bousquet, E. Spaldin, N. & Delaney, K. Unexpectedly Large Electronic Contribution to Linear Magnetoelectricity *Phys. Rev. Lett.* **106**, 107202 (2011).
- [11] Oka, T. & Kitamura, S. Floquet Engineering of Quantum Materials. *Annu. Rev. Condens. Matter Phys.* **10**, 387-408 (2019).
- [12] Morimoto, T. & Nagaosa, N. Topological nature of non-linear optical effects in solids. *Sci. Adv.* **2**, 5 (2016).
- [13] Shirley, J. Solution of the Schrodinger Equation with a Hamiltonian Periodic in Time *Phys. Rev* **138**, 4B (1965).
- [14] Kimel, A. et al. Ultrafast non-thermal control of magnetization by instantaneous photomagnetic pulses. *Nature* **435**, 655-657 (2005).
- [15] Baranga, A. et al. Observation of the inverse Cotton-Mouton effect. *Europhysics Letters* **84**, 44005 (2011).
- [16] Shan, J. et al. Giant modulation of optical nonlinearity by Floquet engineering *Nature* **600**, 235-239 (2021).
- [17] Sie, E. et al. Valley-selective optical Stark effect in monolayer WS_2 . *Nat. Mater.* **14**, 290-294 (2015).
- [18] Sie, E. et al. Large, valley-exclusive Bloch-Siegert shift in monolayer WS_2 . *Science* **355**, 6329 (2015).
- [19] Wang, Y. et al. Observation of Floquet-Bloch States on the Surface of a Topological Insulator *Science* **342**, 453-457 (2013).
- [20] Mahmood, F. et al. Selective scattering between Floquet-Bloch and Volkov states in a topological insulator. *Nat. Phys.* **12**, 306-310 (2016).
- [21] Sirica, N. et al. Photocurrent-driven transient symmetry breaking in the Weyl semimetal TaAs. *Nat. Mater.* **21**, 62-66 (2022).
- [22] Sirica, N. et al. Tracking Ultrafast Photocurrents in the Weyl Semimetal TaAs Using THz Emission Spectroscopy. *Phys. Rev. Lett.* **122**, 197401 (2019).
- [23] Boyd, R. Nonlinear optics *Academic press* (2020).
- [24] Bass, M. et al. Optical Rectification. *Phys. Rev. Lett.* **9**, 446 (1962).
- [25] Harter, J. et al. A parity breaking electronic nematic phase transition in the spin orbit coupled metal $\text{Cd}_2\text{Re}_2\text{O}_7$ *Science* **356**, 295-299 (2017).

- [26] Zhao, L. et al. A global inversion-symmetry-broken phase inside the pseudogap region of $\text{YBa}_2\text{Cu}_3\text{O}_y$ *Nat. Phys.* **13**, 250–254 (2017).
- [27] Wu, L. et al. Giant anisotropic nonlinear optical response in transition metal monpnictide Weyl semimetals *Nat. Phys.* **13**, 350–355 (2017).
- [28] He, X. et al. Robust isothermal electric control of exchange bias at room temperature *Nat. Mater.* **9**, 579–585 (2010).
- [29] Fiebig, M., Pavlov, V. & Pisarev, R. Second-harmonic generation as a tool for studying electronic and magnetic structures of crystals: review *J. Opt. Soc. Am. B* **22**, 1, 96–118 (2005).
- [30] Fiebig, M. et al. Second Harmonic Generation and Magnetic-Dipole —Electric-Dipole Interference in Antiferromagnetic Cr_2O_3 *Phys. Rev. Lett.* **73**, 2127 (1994).
- [31] Sugano, S. & Kojima, N. Magneto-optics *Springer* **128**, (2013).
- [32] Muthukumar, V., Valentí, R. & Gros, C. Microscopic Model of Nonreciprocal Optical Effects in Cr_2O_3 *Phys. Rev. Lett.* **75**, 2766 2766 (1995).
- [33] Muto, M. et al. Magnetoelectric and second-harmonic spectra in antiferromagnetic Cr_2O_3 *Phys. Rev. B* **57**, 9586 (1998).
- [34] Muthukumar, V., Valentí, R. & Gros, C. Theory of non-reciprocal optical effects in antiferromagnets: The case of Cr_2O_3 *Phys. Rev. B* **54**, 433 (1996).
- [35] Krichevstov, B. et al. Magnetoelectric Spectroscopy of Electronic Transitions in Antiferromagnetic Cr_2O_3 *Phys. Rev. Lett.* **76**, 4628 (1996).
- [36] Malashevich, A. et al. Full magnetoelectric response of Cr_2O_3 from first principles *Phys. Rev. Lett.* **86**, 094430 (2012).
- [37] Iyama, A. et al. Magnetoelectric hysteresis loops in Cr_2O_3 at room temperature *Phys. Rev. Lett.* **87**, 180408 (2013).
- [38] Pisarev, R. Crystal optics of magnetoelectrics *Ferroelectrics* **162**, 191–209 (1994).
- [39] Hayashida, T. et al. Observation of antiferromagnetic domains in Cr_2O_3 using nonreciprocal optical effects *Phys. Rev. Res.* **4**, 043063 (2022).
- [40] Satoh, T. et al. Ultrafast spin and lattice dynamics in antiferromagnetic Cr_2O_3 *Phys. Rev. B* **75**, 155406 (2007).
- [41] Satoh, T. et al. Time-resolved demagnetization in Cr_2O_3 by phase sensitive second harmonic generation *Phys. Rev. B* **310**, 1604–1606 (2007).
- [42] Sala, V. et al. Resonant optical control of the structural distortions that drive ultrafast demagnetization in Cr_2O_3 *Phys. Rev. B* **94**, 014430 (2015).
- [43] Birss, R. Symmetry and Magnetism *North Holland*, (1966).
- [44] Fiebig, M., Fröhlich, D. & Sluyterman, G. Domain topography of antiferromagnetic Cr_2O_3 by second-harmonic generation *Appl. Phys. Lett.* **66**, 2906 (1995).
- [45] Kirilyuk, A., Kimel, A. & Rasing, T. Ultrafast optical manipulation of magnetic order *Rev. Mod. Phys.* **82**, 2731 (2010).
- [46] Khomskii, D. Classifying multiferroics: mechanisms and effects. *Physics* **2**, 20 (2009).
- [47] Tokura, Y., Seki, S. & Nagaosa, N. Multiferroics of spin origin. *Rep. Prog. Phys.* **77**, 076501 (2014).

Manipulating the electronic polarization in a magnetoelectric antiferromagnet via the two-photon Stark effect

Xinshu Zhang,¹ Tyler Carbin,¹ Adrian B. Culver,^{1,2} Kai Du,³ Kefeng Wang,³ Sang-Wook Cheong,³ Rahul Roy,¹ and Anshul Kogar^{1,*}

¹*Department of Physics and Astronomy, University of California Los Angeles, Los Angeles, CA 90095, USA*

²*Mani L. Bhaumik Institute for Theoretical Physics, Department of Physics and Astronomy, University of California Los Angeles, Los Angeles, CA 90095, USA*

³*Rutgers Center for Emergent Materials, Rutgers University, Piscataway, NJ, USA*

(Dated: July 25, 2023)

I. ANALYSIS OF EQUILIBRIUM SHG

A. Rotational anisotropy SHG

Radiation can come from various sources, including electric dipoles, magnetic dipoles, electric quadrupoles, and higher order radiation sources. In Cr_2O_3 , magnetic and electric dipole radiation are known to dominate the response. The total source term entering Maxwell's equations is given by

$$\mathbf{S} = \left(\nabla \times \frac{\partial \mathbf{M}}{\partial t} + \frac{\partial^2 \mathbf{P}}{\partial t^2} \right). \quad (\text{S1})$$

The second harmonic intensity measured by the detector in our experiment is $I \propto |\mathbf{e}(2\omega) \cdot \mathbf{S}|^2$, where $\mathbf{e}(2\omega)$ is the unit vector of the output polarizer that selects second harmonic light of a particular polarization. The magnetization at the second harmonic frequency is allowed at all temperatures and has the form of $\mathbf{M}(2\omega) = \chi^m \mathbf{E}(\omega) \mathbf{E}(\omega)$, where χ^m is the second order nonlinear magnetic susceptibility tensor. The electric polarization at the second harmonic frequency is allowed only below T_N and is given by $\mathbf{P}(2\omega) = \chi^e \mathbf{E}(\omega) \mathbf{E}(\omega)$. Below T_N , we can write the SHG intensity as $I \propto |M(\bar{3}m) + P(\bar{3}m)|^2$, where $M(\bar{3}m)$ and $P(\bar{3}m)$ represent the magnetic and electric dipole contributions to SHG signal at a particular polarization angle. Additionally, $\bar{3}m$ is the magnetic point group of the crystal. For light along z -direction (optical axis of the crystal), the electric and magnetic susceptibility tensors have the same independent tensor elements with the relation $\chi_{yyy} = -\chi_{yxx} = -\chi_{xyx} = -\chi_{xxy} = \chi^{e/m}$. By taking the polarization of both the incident fundamental light and the outgoing SHG light into account, we obtain the magnetic dipole contribution, $M(\bar{3}m) \propto \chi^m \sin(3\theta)$, and the electric dipole contribution, $P(\bar{3}m) \propto \chi^e \cos(3\theta)$, where θ is taken to be with respect to the y -axis. The maximum of the magnetic contribution, $M(\bar{3}m)$, is rotated by 90 degrees with respect to the electric contribution, $P(\bar{3}m)$, because of the curl operation in the source term. Above T_N , the SHG data can be described by just magnetic contribution, while below T_N , both electric and magnetic contributions are required to fit the data. χ^m and χ^e are complex quantities, but only the relative phase between them is important. The relative phase can be obtained by two methods. First, it can be obtained directly from the fit of the rotational anisotropy second harmonic generation (RA-SHG) patterns. The electric and magnetic contribution have roughly an 85 degree phase difference at 1180 nm (the wavelength used in the main manuscript) due to local field effects. The fact that the nodes are lifted below T_N is due to this relative phase between the two contributions. Second, the phase can be computed using intensity of the left and right circularly polarized second harmonic emission in combination with intensity of the linearly polarized second harmonic emission as shown in the following section.

B. Left and right circular probe

In this section, we show the two AFM domains can be distinguished at equilibrium by using left and right circularly polarized incident light. Compared to rotational anisotropy SHG measurements, here we replace the polarizer for the

*Electronic address: anshulkogar@physics.ucla.edu

incident light with a quarter wave plate that can generate circularly polarized light. We also remove the analyzer for the second harmonic light. The source term in linear basis is given by

$$\mathbf{S} \propto \left(\nabla \times \frac{\partial \mathbf{M}}{\partial t} + \frac{\partial^2 \mathbf{P}}{\partial t^2} \right) \propto \begin{pmatrix} \chi^m(E_x^2 - E_y^2) + 2\chi^e E_x E_y \\ \chi^e(E_x^2 - E_y^2) - 2\chi^m E_x E_y \\ 0 \end{pmatrix}$$

We can convert the source term into circular basis with $\mathbf{E} = E_R \mathbf{e}_R + E_L \mathbf{e}_L + E_z \mathbf{e}_z$, where $\mathbf{e}_R = -1/\sqrt{2}(\mathbf{e}_x + i\mathbf{e}_y)$ and $\mathbf{e}_L = 1/\sqrt{2}(\mathbf{e}_x - i\mathbf{e}_y)$. Then one gets

$$\mathbf{S} = \begin{pmatrix} S_R \\ S_L \\ S_z \end{pmatrix} \propto \begin{pmatrix} (-\chi^m + i\chi^e)E_L^2 \\ (\chi^m + i\chi^e)E_R^2 \\ 0 \end{pmatrix}$$

$I_{R/L} \propto |\mathbf{S}|^2$. Hence, the SHG intensity is

$$I_{R/L} \propto (|\chi^m|^2 + |\chi^e|^2) \mp 2(|\chi^m||\chi^e|)\sin(\gamma), \quad (\text{S2})$$

where γ is the phase difference between χ^m and χ^e . The first term is quadratic in χ^m and χ^e and is always positive, while the second term is the so-called interference term and may be positive or negative. The sign of the interference term can be switched either by changing the handedness of the circular light or by probing the opposite antiferromagnetic domain. Additionally, the interference is also affected by the wavelength of the probe. The largest contrast in the second harmonic response to the incident left and right circularly polarized light occurs when the magnitude of χ^m and χ^e are the same and possess a 90 degree phase difference.

C. Computing the relative phase

The relative phase between χ^m and χ^e can be obtained either from directly fitting the SHG pattern or derived from Eq. S2 as

$$\gamma = \sin^{-1} \left(\frac{I_R - I_L}{I_R + I_L} \cdot \frac{I_M + I_E}{2\sqrt{I_M I_E}} \right). \quad (\text{S3})$$

Here, the I_R and I_L denote the SHG intensities due to right and left circularly polarized light, and I_M and I_E denote the SHG intensities due to the magnetic dipole and electric dipole radiation (i.e. $\propto |\chi^m|^2$ and $|\chi^e|^2$), respectively. The phase obtained using both this method and fitting the RA-SHG patterns are consistent.

II. ANALYSIS OF NON-EQUILIBRIUM SHG

A. Derivation of the -2ϕ in optical rectification process

The optical rectification caused by the pump is given by $\mathbf{P}(\omega_0) = \chi_{OR}^e \mathbf{E}^p(\omega) \mathbf{E}^p(-\omega)$. Under the magnetic point group symmetry $\bar{3}m$, the relevant susceptibility tensor elements are $\chi_{yyy} = -\chi_{yxx} = -\chi_{xyx} = -\chi_{xxy} = \chi_{OR}^e$. The light induced polarization can be decomposed into x and y components $\mathbf{P}(\omega_0) = P_x \mathbf{e}_x + P_y \mathbf{e}_y$ with $P_x = 2\chi_{xyx} E_y E_x$ and $P_y = \chi_{yyy} E_y E_y + \chi_{yxx} E_x E_x$. For a linearly polarized pump we have $E_x = E^p \sin\phi$ and $E_y = E^p \cos\phi$, where the E^p is the magnitude of the electric field from the pump and the ϕ is the angle between the pump polarization and the y -axis, as defined in the main text. Therefore, we obtain

$$\mathbf{P}(\omega_0) = \chi_{OR}^e (E^p)^2 [\sin(-2\phi) \mathbf{e}_x + \cos(-2\phi) \mathbf{e}_y] \quad (\text{S4})$$

B. Functional form of pump induced electric and magnetic dipole contributions to the second harmonic intensity

The pump induced nonlinear magnetization and polarization are given by

$$\begin{aligned} \mathbf{M}^p(2\omega) &= \chi^m \mathbf{E}(\omega) \mathbf{E}(\omega) \mathbf{P}(\omega_0) \\ \mathbf{P}^p(2\omega) &= \chi^e \mathbf{E}(\omega) \mathbf{E}(\omega) \mathbf{P}(\omega_0), \end{aligned} \quad (\text{S5})$$

where the $\chi^{e/m}$ are third order susceptibility tensors constrained by the $\bar{3}m$ symmetry. The pump gives rise to additional contributions to the second order susceptibility tensors $\delta\chi_{ijk}^m = \chi_{ijkl}^m P_l(\omega_0)$ and $\delta\chi_{ijk}^e = \chi_{ijkl}^e P_l(\omega_0)$ that modify the equilibrium tensors, χ_{ijk}^m and χ_{ijk}^e . When the pump and probe are normally incident on the sample, only eight matrix elements of the second order tensor, χ_{ijk} , are experimentally accessible. The tensor elements related to the z components can be ignored. We can then write the effective equilibrium second order susceptibility tensor as:

$$\chi^{e/m} = \begin{pmatrix} 0 & -\chi^{e/m} \\ -\chi^{e/m} & 0 \\ -\chi^{e/m} & 0 \\ 0 & \chi^{e/m} \end{pmatrix}$$

When considering the effect of the pump, we therefore need to consider only eight tensor elements of $\chi_{ijkl}^{e/m}$:

$$\begin{cases} \chi_{xxyy} = \chi_{yyxx} \\ \chi_{xyyx} = \chi_{yxxy} \\ \chi_{xyxy} = \chi_{yxyx} \\ \chi_{xxxx} = \chi_{yyyy} = \chi_{xxyy} + \chi_{xyyx} + \chi_{xyxy} \end{cases}$$

The perturbation due to induced polarization can then be included into an effective second order susceptibility tensor by writing:

$$\delta\chi^{e/m} = \begin{pmatrix} \chi_{xxxx} \cdot P_x & \chi_{xyxy} \cdot P_y \\ \chi_{xxyy} \cdot P_y & \chi_{xyyx} \cdot P_x \\ \chi_{yxxy} \cdot P_y & \chi_{yyxx} \cdot P_x \\ \chi_{yxyx} \cdot P_x & \chi_{yyyy} \cdot P_y \end{pmatrix}$$

From the previous section, we have $\mathbf{P}(\omega_0) = P_x \mathbf{e}_x + P_y \mathbf{e}_y = \chi_{OR}^e (E^p)^2 [\sin(-2\phi) \mathbf{e}_x + \cos(-2\phi) \mathbf{e}_y]$. Then we obtain the $M(C_2) \propto \delta\chi^m \sin(\theta - 2\phi)$ and $P(C_2) \propto \delta\chi^e \cos(\theta - 2\phi)$ as mentioned in the main text, where $\delta\chi^m \propto \chi_{yyyy}^m \chi_{OR}^e (E^p)^2$ and $\delta\chi^e \propto \chi_{yyyy}^e \chi_{OR}^e (E^p)^2$. In summary, we have

$$\begin{aligned} I(2\omega; \varphi) \propto & |e^{i\gamma} \chi^m \sin(3\theta) + \chi^e \cos(3\theta) \\ & + ie^{i\gamma} \delta\chi^m \sin(\theta - 2\varphi) + i\delta\chi^e \cos(\theta - 2\varphi)|^2. \end{aligned} \quad (S6)$$

C. Property of susceptibility tensors and complexity of each contribution

For physical fields, $A(t)$, we have $\Theta A(t) = \pm A(t)$, where Θ represents the time reversal operator. The “+” sign corresponds to i-type fields and “−” sign to c-type fields. In the Fourier domain, we get the corresponding relationship: $\Theta A(\omega) = \pm A^*(\omega)$. In Cr_2O_3 , below T_N , inversion and time reversal symmetry are both broken by the antiferromagnetic arrangement of spins, but the combined symmetry of inversion and time reversal remains a symmetry element *in the absence of dissipation*. Hence we have

$$\Theta \mathbf{I} \chi^{e/m} = \chi^{e/m}, \quad (S7)$$

where Θ and \mathbf{I} are the time reversal and inversion operators, respectively. Applying the combined time reversal and inversion operators $\Theta \mathbf{I}$ to $\mathbf{P}(\omega_0) = \chi_{OR}^e \mathbf{E}(\omega_1) \mathbf{E}(-\omega_2)$, we get $-\mathbf{P}^*(\omega_0) = \chi_{OR}^e (-\mathbf{E}^*(\omega)) (-\mathbf{E}^*(\omega))$, where we have used Eq. S7. After taking the complex conjugate of this equation, we get $\mathbf{P}(\omega_0) = -(\chi_{OR}^e)^* \mathbf{E}(\omega_1) \mathbf{E}(-\omega_2)$. The susceptibility tensor describing optical rectification is then constrained to obey $\chi_{OR}^e = -(\chi_{OR}^e)^*$, indicating χ_{OR}^e is purely imaginary. Therefore, in the absence of dissipation (as satisfied by pumping below the gap), the light-induced polarization $\mathbf{P}(\omega_0)$ is purely imaginary, and $\delta\chi^e$ ($\delta\chi^m$) and χ^e (χ^m) must possess a 90 degree phase difference. This is consistent with our results and can explain the domain contrast observed upon pumping.

Above the Néel temperature T_N , Cr_2O_3 possesses symmetries of the centrosymmetric point group $\bar{3}m$. Axial i-type tensors of odd rank, such as χ_{ijk}^m , and polar i-type tensors of even rank, such as χ_{ijkl}^e , are allowed. Below T_N , inversion symmetry is broken due to the spin arrangement and the magnetic point group of Cr_2O_3 is $\bar{3}m$. In addition to χ_{ijk}^m and χ_{ijkl}^e , polar c-type tensors of odd rank, such as χ_{ijk}^e , and axial c-type tensors of even rank, such as χ_{ijkl}^m , become allowed. Both of these tensors are proportional to the order parameter (i.e. the Néel vector) and flip sign when examining opposite AFM domains. Therefore, $\delta\chi^e$ is an axial c-type tensor and $\delta\chi^m$ is a polar i-type tensor. Hence, $\delta\chi^e$ flips sign when examining opposite antiferromagnetic domains, while $\delta\chi^m$ remains unchanged.

III. TEMPERATURE DEPENDENCE OF SHG

In this section, we present pumped and unpumped RA-SHG patterns at various temperatures, and show that the pump induced susceptibility tensor $\delta\chi^e$ has an order parameter-like behavior as a function of temperature. We plot the unpumped and pumped SHG patterns in Fig. S1 at five selected temperatures close to $T_N \sim 307$ K. Laser heating increases the sample temperature by roughly 3-5 K. Therefore, for the 305 K data, the actual temperature is above T_N as evidenced by the appearance of the nodes in RA-SHG pattern (and equal SHG intensities when examining the left and right circularly polarized SHG signals). From our fits, we can extract χ^e from the unpumped data and $\delta\chi^e$ from the pumped data at each temperature. In Fig. S2, we present χ^e and $\delta\chi^e$ versus temperature. We find that, consistent with previous studies, χ^e is proportional to the Néel vector. The critical exponent of the order parameter $\beta \approx 0.32$. In the previous section we showed that $\delta\chi^e \propto \chi_{yyy}^e \chi_{OR}^e$, which indicates that $\delta\chi^e$ is also related to the order parameter and should also disappear above T_N . Under the assumption that the i-type tensor element χ_{yyy}^e is constant across the AFM transition, $\delta\chi^e$ is linearly proportional to the order parameter. It should be kept in mind, however, that χ_{yyy}^e may scale quadratically with the order parameter. From our data alone, it is difficult to ascertain whether $\delta\chi^e$ is linearly proportional to the order parameter due to the large measurement uncertainty. The best fit gives rise to an exponent $\beta \sim 0.5$, but $\beta \sim 0.32$ also falls within the error bars. Nevertheless, the pump induced $\delta\chi^e$ is related to the order parameter and should flip signs as switching to the other domain.

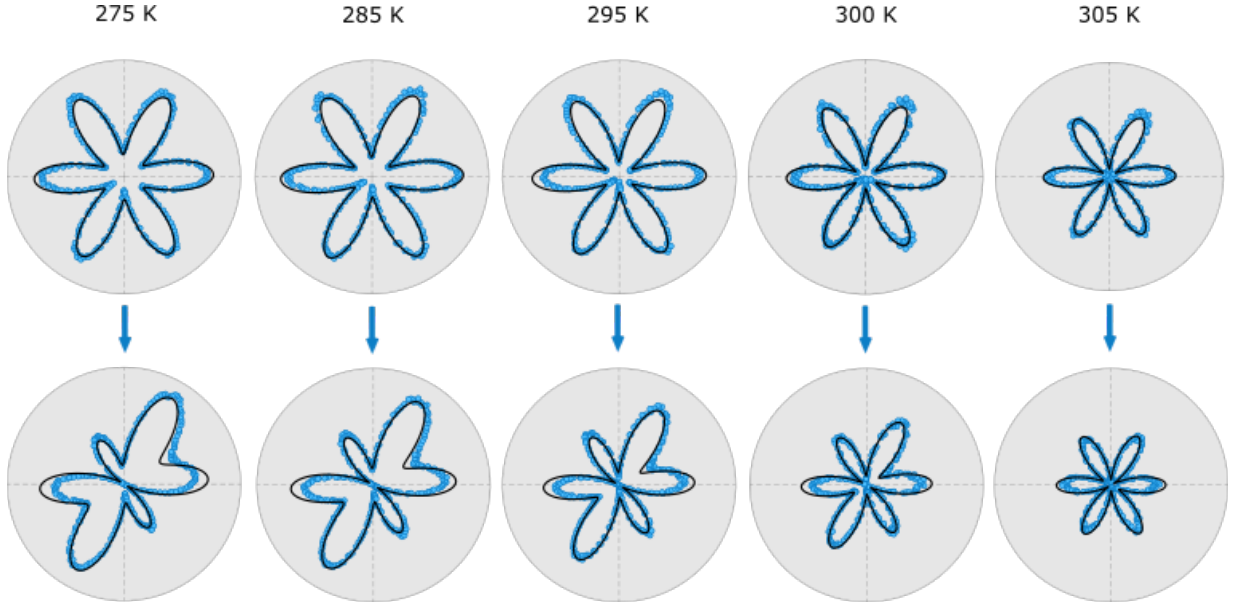


FIG. S1 Top row: unpumped SHG pattern of β domain at various temperatures. Bottom row: pumped SHG pattern taken at time zero at various temperatures.

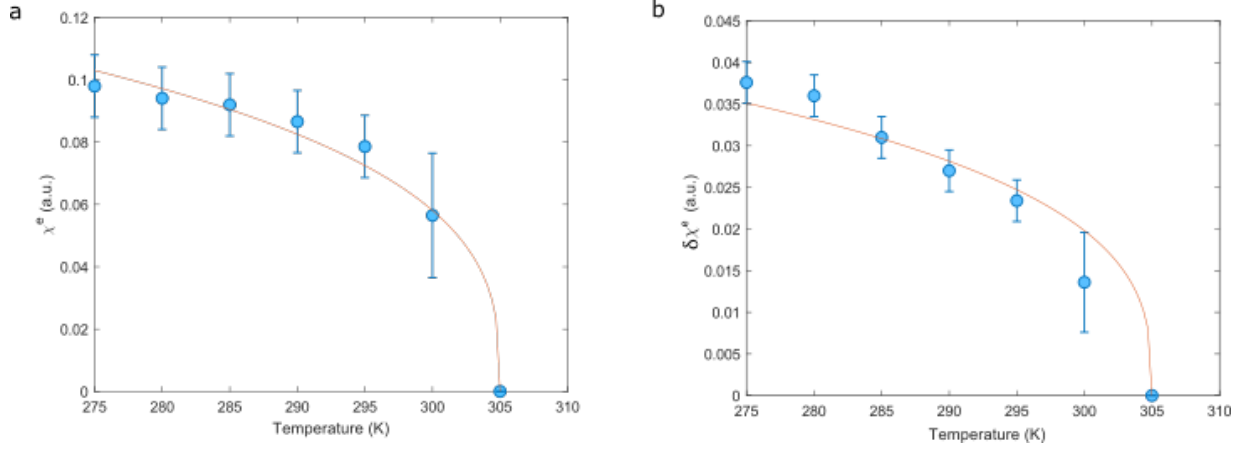


FIG. S2 (a) χ^e versus temperature. The solid curve is the fit using $a(T - T_c)^\beta$, the obtained $\beta \sim 0.32$ is consistent with previous results, confirming the c type tensor χ_{ijk}^e is proportional to order parameter. (b) $\delta\chi^e$ versus temperatures. The solid line is fitting by fixing $\beta = 0.32$.

IV. SHG IN THE PERPENDICULAR CHANNEL

In the main text and previous section, we showed data with the two polarizers (for the incident and outgoing light) in a parallel geometry. Here, we show the data in the perpendicular geometry. In our setup, we rotate the half wave plate so that the input polarization is rotated by 90 degrees to achieve the perpendicular geometry. In contrast to the parallel geometry, we now get $M(\bar{3}m) \propto \chi^m \cos(3\theta)$ and $P(\bar{3}m) \propto \chi^e \sin(3\theta)$ for the equilibrium RA-SHG pattern, while the terms $M(C_2) \propto \delta\chi^m \cos(\theta - 2\phi)$ and $P(C_2) \propto \delta\chi^e \sin(\theta - 2\phi)$ need to be included upon pumping. In the perpendicular channel, $\delta\chi^m \propto \chi_{yxxy}^m \chi_{OR}^e (E^p)^2$ and $\delta\chi^e \propto \chi_{yxxy}^e \chi_{OR}^e (E^p)^2$. Fig. S3 shows the unpumped RA-SHG pattern with a fundamental probe wavelength of 1180 nm in the perpendicular channel. This figure also shows the corresponding pumped RA-SHG pattern with pump polarization along the x axis. Fig. S4 shows the pumped RA-SHG pattern as the pump polarization is rotated clockwise in 20 degree steps. Again, these are not fits to the individual RA-SHG patterns – instead, only the $\varphi = -90^\circ$ pattern is fit and the black curves pertaining to the remaining RA-SHG patterns are generated from our fit function.

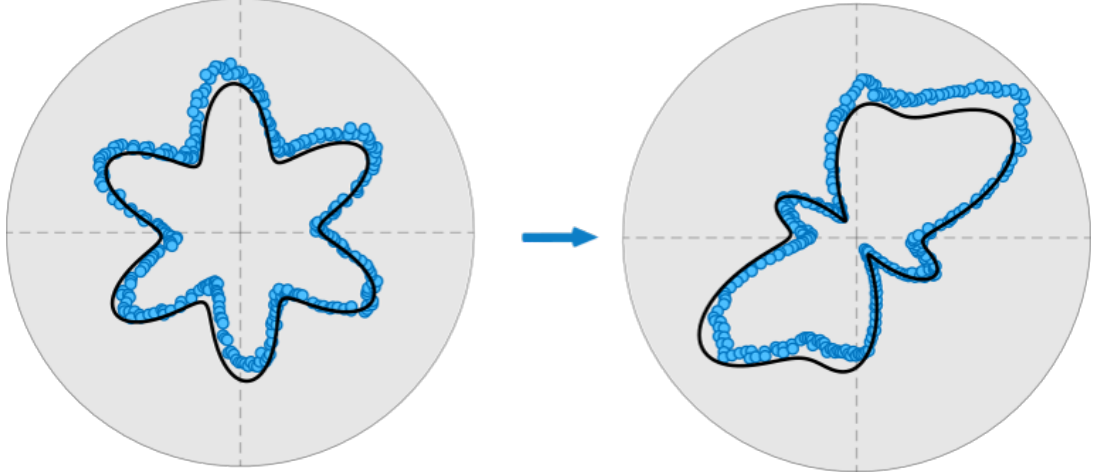


FIG. S3 The equilibrium and non-equilibrium SHG pattern of β domain for perpendicular channel. The probe wavelength 1180 nm and the pump is along x axis.



FIG. S4 The evolution of SHG pattern at time zero for β domain as varying the pump polarization. The pump polarization starting along x axis is rotated clockwise at 20° step size, denoted by the orange double headed arrow. The C_2 symmetry axis is represented by red single headed arrow. Note only the solid black for pump along x is fit, the rest is obtained by varying 2ϕ in opposite direction and keeping all the other parameters the same.

V. EFFECT OF CIRCULAR PUMP

In this section, we demonstrate that a circularly polarized pump pulse does not induce a quasi-static electric dipole in Cr_2O_3 when pumping in the transparency window away from any electronic transitions. This calculation is more easily demonstrated in the time-domain, where we make the assumption that the medium is lossless and dispersionless. We can write that $\tilde{\mathbf{P}}(t) = \chi_{OR}^e \tilde{\mathbf{E}}^p(t) \tilde{\mathbf{E}}^p(t)$, where the tilde denotes a time-dependent quantity. Under the magnetic point group symmetry $\bar{3}m$, the relevant susceptibility tensor elements are $\chi_{yyy} = -\chi_{yxx} = -\chi_{xyx} = -\chi_{xxy} = \chi^{e/m}$. We can write $\tilde{\mathbf{P}}(t) = \tilde{P}_x \mathbf{e}_x + \tilde{P}_y \mathbf{e}_y$, and the x and y components are $\tilde{P}_x = 2\chi_{xyx} \tilde{E}_y \tilde{E}_x$ and $\tilde{P}_y = \chi_{yyy} \tilde{E}_y \tilde{E}_y + \chi_{yxx} \tilde{E}_x \tilde{E}_x$ as in the previous section. Now with a circularly polarized pump, the x and y components of pump electric field are out of phase, and we have (for right circular pump) $\tilde{E}_x = \frac{1}{\sqrt{2}}(E^p)\sin(\omega t)$ and $\tilde{E}_y = \frac{1}{\sqrt{2}}(E^p)\cos(\omega t)$, where the E^p is the electric field from the pump. We obtain

$$\tilde{\mathbf{P}}(t) = \frac{1}{2} \chi_{OR}^e (E^p)^2 [\sin(-2\omega t) \mathbf{e}_x + \cos(-2\omega t) \mathbf{e}_y]. \quad (\text{S8})$$

Because the calculation does not consist of a constant part (i.e. a time-independent contribution), but only a time-dependence at twice the incident frequency, there is no rectified signal. Circularly polarized light only generates second harmonic light, and not optical rectification, in Cr_2O_3 .

In Fig.S5, we show that when the α domain is pumped with circularly polarized light, there is no change in symmetry, consistent with the calculation presented above. The circularly polarized light was generated using quarter wave plate and the fluence used was approximately 20 mJ/cm^2 , the same as that used in the main manuscript with linearly polarized light.

VI. WAVELENGTH DEPENDENCE AND PHASE

In this section, we highlight the key role played by the equilibrium interference between electric and magnetic dipole radiation in observing the symmetry-breaking effects in Cr_2O_3 . As we tune the second harmonic energy across several electronic $d-d$ transitions, the relative phase difference γ between electric and magnetic radiation changes correspondingly, and can be experimentally determined using Eq. S3 and is shown in Fig. S6(d).

In the top panel of Fig. S6(b), we show four equilibrium RA-SHG patterns at representative second harmonic energies corresponding to the dashed vertical lines in Fig.S6(a), (c) and (d). These values were chosen because they constitute extremal values of γ ($\sim 0^\circ$ at 2.56 eV and 2.43 eV, $\sim 90^\circ$ at 2.64 eV and $\sim -90^\circ$ at 2.10 eV). In Fig. S6(b), we show that when $\gamma \approx 0^\circ$, nodes are observed in the equilibrium RA-SHG pattern, and the induced dipole is barely visible when pumped. On the other hand, when $\gamma \approx \pm 90^\circ$, the equilibrium nodes are lifted, and the pump has a dramatic effect on the symmetry of the RA-SHG. That the effect is most drastic at $\gamma \approx \pm 90^\circ$ is also captured by Eq. S6. When $\gamma \neq 0^\circ$, interference between the equilibrium and perturbing terms arise. These interference terms are

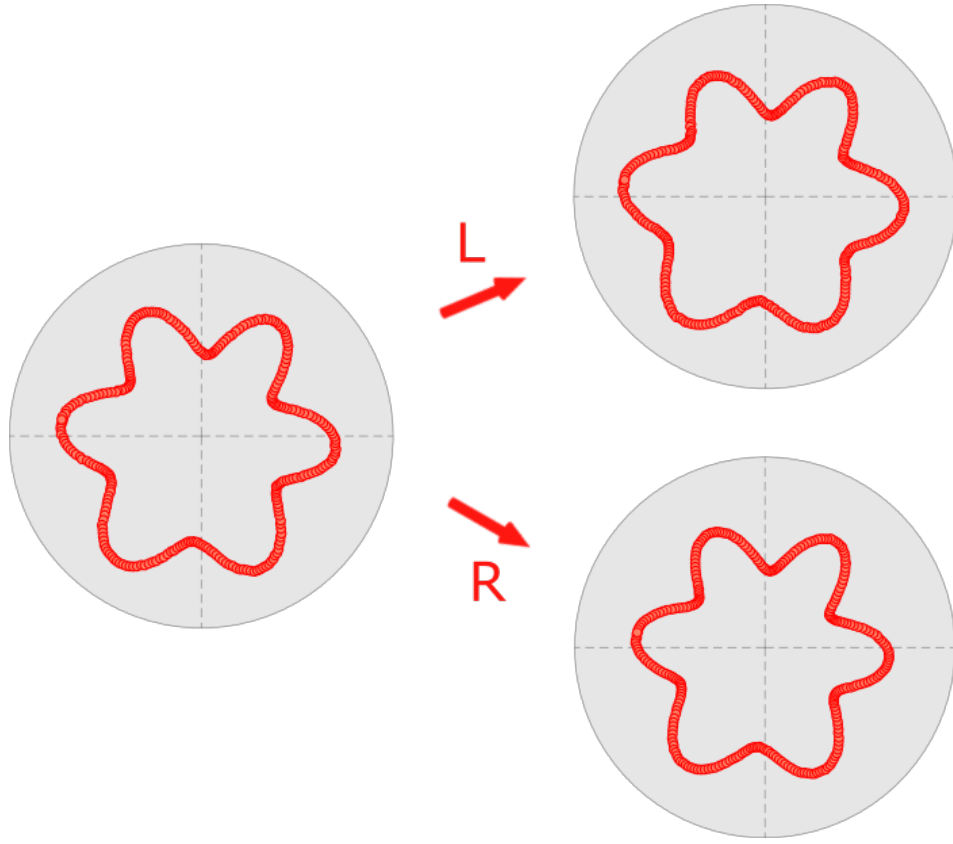


FIG. S5 Both left and right circular pump has minimal change to the SHG pattern of α domain. The probe wavelength is 1180 nm.

linear in $\delta\chi^{e/m}$. In contrast, when $\gamma = 0^\circ$ Eq. S6 factorizes and only terms $\mathcal{O}(\delta^2)$ remain. The lack of interference thus renders the induced dipole imperceptible.

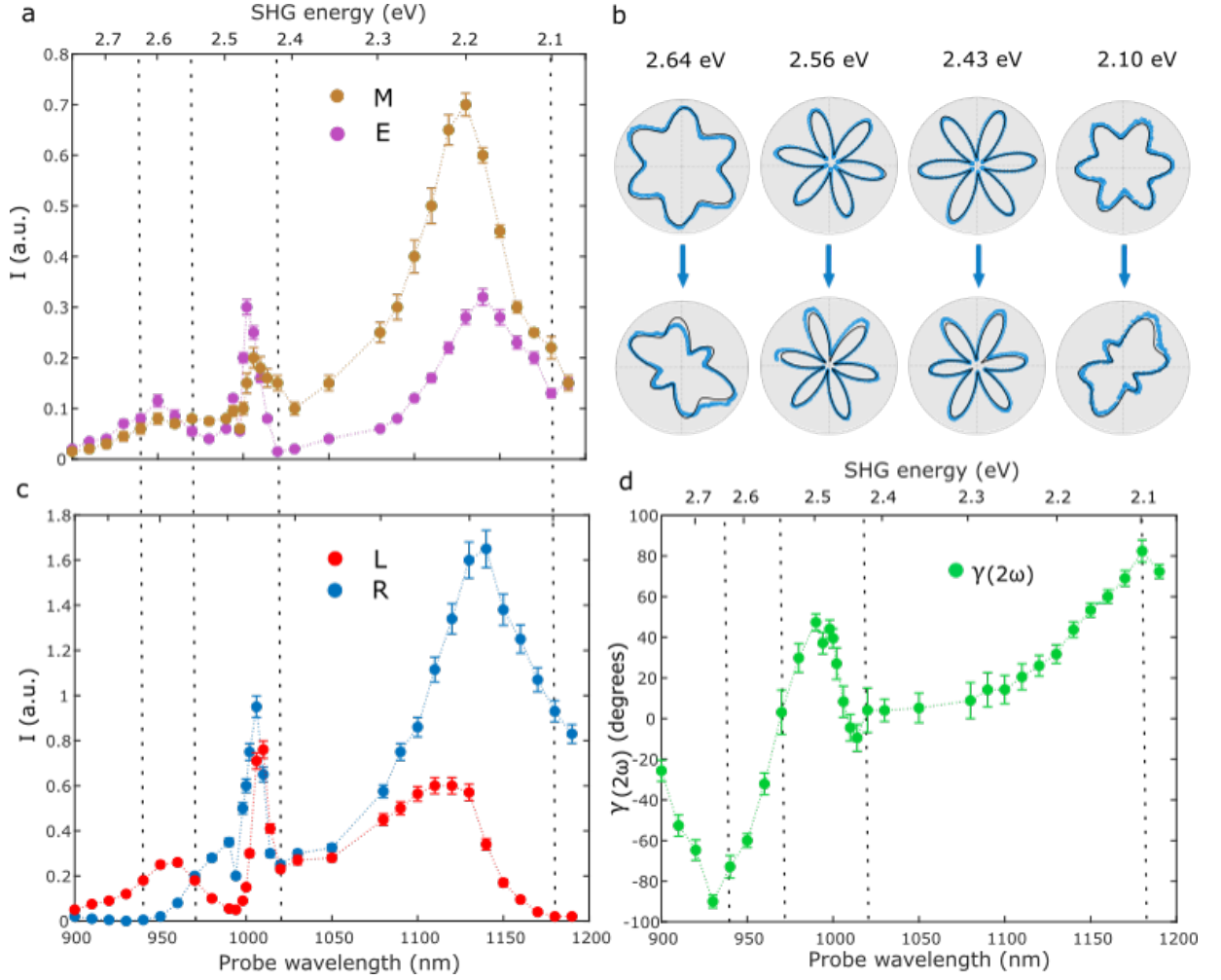


FIG. S6 (a) Wavelength dependence of SHG intensity for magnetic $I_M \propto |M(\bar{3}m)|^2$ and electric contribution and $I_P \propto |P(\bar{3}m)|^2$ at equilibrium, measured with probe polarization set to be along x and y axis, respectively. (b) Unpumped and pumped SHG patterns at four representative wavelengths 940, 970, 1020, 1180 nm, corresponding to SHG energy 2.6, 2.55, 2.4, 2.1 eV. The probe intensity is not calibrated for each SHG pattern. (c) Wavelength dependence of SHG signal probed with left and right circular light at equilibrium. (d) The computed relative phase difference for magnetic and electric radiation. The wavelength dependence measurements were done on β domain.

VII. WAVE-FUNCTIONS FOR MICROSCOPIC MECHANISM OF OPTICAL RECTIFICATION VIA TWO-PHOTON STARK EFFECT

At equilibrium, the ground state $|g\rangle$ in Cr_2O_3 is $^4A_{2g}$, which comprises three electrons in t_{2g} state. The relevant excited states, $|e\rangle$, comprise the $^4T_{2g}$ and $^4T_{1g}$ levels, both of which possess two t_{2g} electrons and one e_g electron. The t_{2g} and e_g states can be constructed based on the $\bar{3}m$ point group symmetry as shown by Eq. S9:

$$\begin{aligned}
 |t_{2g}^{(1)}\rangle &= d_{x^2+y^2} \\
 |t_{2g}^{(2)}\rangle &= ((id_{xy} - d_{x^2-y^2}) + \eta(p_x + ip_y))/(1 + \eta) \\
 |t_{2g}^{(3)}\rangle &= ((id_{xy} + d_{x^2-y^2}) + \eta(-p_x + ip_y))/(1 + \eta) \\
 |e_g^{(2)}\rangle &= ((id_{xy} + d_{x^2-y^2}) + \eta(p_x - ip_y))/(1 + \eta) \\
 |e_g^{(1)}\rangle &= ((id_{xy} - d_{x^2-y^2}) + \eta(-p_x - ip_y))/(1 + \eta)
 \end{aligned} \tag{S9}$$

where, for this choice of basis, z is along the direction of the trigonal elongation, (i.e. the $[111]$ -direction of the

oxygen octahedron). Here, we already take into consideration the mixing of 4p orbitals due to the trigonal field, where η denotes the strength of trigonal distortion and an arbitrary number is used for illustration purposes ($\eta = 0.7$). As will be shown in next section, a single-electron approach is equivalent to multi-electron approach. Therefore the total electric dipole can be obtained by adding up the dipole moments of each single electron. We can draw the corresponding single electron probability densities (in the $x - y$ plane) for $|g\rangle$ and $|e\rangle$ based on the above wave-functions. In the Fig. 4(a), we show the electron probability densities of $(t_{2g}^{(1)}, t_{2g}^{(2)}, t_{2g}^{(3)})$ for $|g\rangle$ and one combination $(t_{2g}^{(1)}, t_{2g}^{(2)}, e_g^{(1)})$ as an example for the $|e\rangle$ manifold.

In the presence of time periodic pump pulse, Floquet states are created and we show only the lowest order (within the rotating wave approximation) $|e, -1\rangle$ state in Fig. 4. There are two pathways that can give rise to a static dipole as explained in the main text. The consequences of these two pathways are the mixing among $(t_{2g}^{(1)}, t_{2g}^{(2)}, t_{2g}^{(3)}, e_g^{(1)}, e_g^{(2)})$ states in terms of the single electron approach. We show a representative electron probability density for the hybridized state $|g, 0\rangle + \epsilon^2 |e, 0\rangle$ (corresponding to the first pathway): $|t_{2g}^{(1)}\rangle \rightarrow |t_{2g}^{(1)} + \zeta(t_{2g}^{(2)} + t_{2g}^{(3)}) + \xi e_g^{(1)}\rangle$, $|t_{2g}^{(2)}\rangle \rightarrow |t_{2g}^{(2)} + \zeta(t_{2g}^{(1)} + t_{2g}^{(3)}) + \xi e_g^{(2)}\rangle$ and $|t_{2g}^{(3)}\rangle \rightarrow |t_{2g}^{(3)} + \zeta(t_{2g}^{(1)} + t_{2g}^{(2)}) + \xi e_g^{(3)}\rangle$. The coefficients characterizing the hybridization strength are determined by transition matrix elements (such as intensity and light polarization). Arbitrary values ξ and ζ are chosen for illustration purposes, as shown in Fig.4 in the main text (e.g., $\zeta = 0.1$ and $\xi = 0.2$). As shown in Fig.4, the hybridized states break the threefold in-plane rotational symmetry and can give rise to the light-induced electronic dipole moment.

VIII. PERTURBATIVE CALCULATION OF DIPOLE MOMENT

We set up a toy model for the pumped Cr_2O_3 and calculate the static dipole moment using time-dependent perturbation theory. Then, we repeat the same calculation using the Floquet approach. Finally, we show that the same answer must be obtained if the dipole moment is written as the sum of dipole moments in time-evolving single-electron states.

1. Time-dependent perturbation theory

We consider an atomic model consisting of a non-degenerate ground state $|0\rangle$ at energy w_0 (we set $\hbar = 1$ throughout) and excited states $|1\rangle, \dots, |N\rangle$ at energy $w_1 = \dots = w_N > w_0$, with dipole coupling to light. Thus, we consider

$$H(t) = H^{(0)} + H^{(1)}(t), \quad (\text{S10})$$

where $H^{(0)}$ is the unperturbed Hamiltonian and $H^{(1)}(t)$ is the dipole coupling to the pump field $\mathbf{E}(t)$:

$$H^{(0)} = \sum_{i=0}^N w_i |i\rangle \langle i| \quad (\text{S11a})$$

$$H^{(1)}(t) = -\mathbf{d} \cdot \mathbf{E}(t). \quad (\text{S11b})$$

We do not include dissipation because the experiment was done in a regime without significant absorption.

Setting $N = 6$ corresponds to a toy model of a given Cr atom in Cr_2O_3 . The ground state is the $^4A_{2g}$ state ($|g\rangle$ in the main text), and the only excited states kept are the three $^4T_{1g}$ states and the three $^4T_{2g}$ states ($|e\rangle$ in the main text). We need not consider excited states that flip the spin because they are dipole forbidden. In this toy model, we assume that the six excited states are exactly degenerate. While the energy splitting (approximately 0.5 eV) between the $^4T_{1g}$ states and $^4T_{2g}$ states may have a non-negligible quantitative effect on the static dipole moment, we set this splitting to zero as a simplifying assumption to convey the basic idea. Non-zero splitting can be included straightforwardly in this approach.

A perturbative treatment of $H^{(1)}$ is appropriate because the linear dependence on fluence [Fig. 4(b) in the main text] indicates that the static dipole depends quadratically on the electric field amplitude. Also, we can roughly estimate the electric field amplitude E from the fluence $f = 20 \text{ mJ/cm}^2$ via $f \approx |\frac{1}{\mu_0} \mathbf{E} \times \mathbf{B}| t_{\text{pulse}} = c\epsilon_0 E^2 t_{\text{pulse}}$ (where $t_{\text{pulse}} = 190 \text{ fs}$), yielding $E \approx 6 * 10^8 \text{ V/m}$. Then, estimating the dipole moment as the electron charge times the Bohr radius, we obtain the order of magnitude of $H^{(1)}(t)$ as 0.06 eV, which is small compared to $w_2 - w_1 = 2.1 \text{ eV}$ (the energy gap between $^4T_{1g}$ and $^4A_{2g}$).

We take the electric field $\mathbf{E}(t)$ of the pump pulse to be linearly polarized:

$$\mathbf{E}(t) = \varphi(t)\mathbf{E} = \int \frac{dw}{2\pi} e^{-iwt} \varphi(w)\mathbf{E}, \quad (\text{S12})$$

where \mathbf{E} is a fixed vector defining the polarization axis, $\varphi(t)$ is the time dependence of pump pulse, and $\varphi(w) = \int dt e^{iwt} \varphi(t)$ is the pump pulse in the frequency domain.

Since $\varphi(t)$ must be real, $\varphi(w) = \varphi^*(-w)$; we therefore focus on $w > 0$ in the following discussion of the pump pulse. We take $\varphi(w)$ to be sharply peaked, with some pulse width Δ , about the laser frequency Ω ; in particular, we assume

$$\varphi(w) \xrightarrow{\Delta \rightarrow 0^+} \pi \delta(w - \Omega) \quad (w > 0). \quad (\text{S13})$$

Thus, $\varphi(t) \xrightarrow{\Delta \rightarrow 0^+} \cos(\Omega t)$, while for small $\Delta > 0$, $\varphi(t)$ is a broad wave train at frequency Ω that goes to zero at $t \rightarrow \pm\infty$. We are interested in time t in the broad middle of the wave train. For simplicity, we assume that $\varphi(w)$ is strictly zero for w outside of $[\Omega - \frac{1}{2}\Delta, \Omega + \frac{1}{2}\Delta]$.

We consider evolving the system starting from the ground state at time t_0 (later sending $t_0 \rightarrow -\infty$). We wish to calculate the dipole moment at a time t :

$$\langle \mathbf{d} \rangle_t \equiv \langle \Psi(t) | \mathbf{d} | \Psi(t) \rangle, \quad (\text{S14})$$

where

$$|\Psi(t)\rangle = U(t, t_0) |0\rangle = \sum_{i=0}^N a_i(t) |i\rangle. \quad (\text{S15})$$

We calculate the coefficients $a_i(t)$ perturbatively:

$$a_i(t) = a_i^{(0)}(t) + a_i^{(1)}(t) + a_i^{(2)}(t) + \dots, \quad (\text{S16})$$

where the superscripts indicate the order in $|\mathbf{E}|$. It is convenient to first calculate the coefficients in the interaction picture (relative to $t = t_0$), i.e., to define

$$a_{i,I}(t) = e^{i w_i(t-t_0)} a_i(t). \quad (\text{S17})$$

The interaction picture coefficients are determined order-by-order by $a_{i,I}^{(n)}(t_0) = \delta_{i0} \delta_{n0}$ and

$$i \frac{d}{dt} a_{i,I}^{(n+1)}(t) = \sum_{j=0}^N [H_I^{(1)}(t)]_{ij} a_{j,I}^{(n)}(t) \quad (\text{S18a})$$

$$= - \sum_{j=0}^N \mathbf{d}_{ij} \cdot \mathbf{E} \varphi(t) e^{i(w_i - w_j)(t-t_0)} a_{j,I}^{(n)}(t), \quad (\text{S18b})$$

where we use the notation $\mathcal{O}_{ij} = \langle i | \mathcal{O} | j \rangle$ for the matrix elements of any operator \mathcal{O} .

Throughout this calculation, we always take the vector \mathbf{d} to be in-plane (x - y). This is justified because the pump field was polarized in-plane [hence only the in-plane components of \mathbf{d} appear in $H^{(1)}(t)$] and because the measurement could only detect in-plane components of \mathbf{d} [hence we only need to calculate $\langle \mathbf{d} \rangle_t$ in-plane]. Due to the C_3 site symmetry of the Cr atom, the in-plane components of the dipole vanish in the ground state:

$$\mathbf{d}_{00} = \mathbf{0}. \quad (\text{S19})$$

We work to second order in $|\mathbf{E}|$ because, as we will see, this yields the leading contribution to the static part of the dipole moment. Once the $a_i(t)$ coefficients are determined up to second order, the dipole moment is obtained as

$$\langle \mathbf{d} \rangle_t = \langle \mathbf{d} \rangle_t^{(0)} + \langle \mathbf{d} \rangle_t^{(1)} + \langle \mathbf{d} \rangle_t^{(2)} + \dots, \quad (\text{S20})$$

where one finds, after noting $a_i^{(0)}(t) = \delta_{i0} e^{-iE_0(t-t_0)}$ and $\mathbf{d}_{00} = \mathbf{0}$ [which imply $a_0^{(1)}(t) = 0$],

$$\langle \mathbf{d} \rangle_t^{(0)} = \mathbf{0}, \quad (\text{S21a})$$

$$\langle \mathbf{d} \rangle_t^{(1)} = 2 \sum_{i=1}^N \text{Re} \left(e^{i w_0(t-t_0)} \mathbf{d}_{0i} a_i^{(1)}(t) \right), \quad (\text{S21b})$$

$$\langle \mathbf{d} \rangle_t^{(2)} = \sum_{i,j=1}^N a_i^{(1)*}(t) \mathbf{d}_{ij} a_j^{(1)}(t) + 2 \sum_{i=1}^N \text{Re} \left(e^{i w_0(t-t_0)} \mathbf{d}_{0i} a_i^{(2)}(t) \right). \quad (\text{S21c})$$

We send the start time $t_0 \rightarrow -\infty$ before sending the pulse width to zero ($\Delta \rightarrow 0^+$). We take these limits with the observation time t held fixed so that t is in the broad middle of the wave train ($\Delta|t| \ll 1$). We send the pulse width to zero to yield an approximate answer that is independent of the particular way the pulse turns on and off in time. This results in some contributions to $\langle \mathbf{d} \rangle_t$ being strictly static. If we instead were to keep a small non-vanishing pulse width, then additional quasistatic contributions would appear (with frequencies no larger than the pulse width) that depend on further details of how the pulse turns on and off in time.

We readily obtain the first-order correction to the wavefunction:

$$a_i^{(1)}(t) \xrightarrow{t_0 \rightarrow -\infty} e^{-i w_0(t-t_0)} \mathbf{d}_{i0} \cdot \mathbf{E} \int \frac{dw}{2\pi} \frac{1}{w_i - w_0 - w} e^{-i w t} \varphi(w) \quad (\text{S22a})$$

$$\xrightarrow{\Delta \rightarrow 0^+} e^{-i w_0(t-t_0)} \mathbf{d}_{i0} \cdot \mathbf{E} \frac{1}{2} \left(\frac{1}{w_i - w_0 - \Omega} e^{-i \Omega t} + \frac{1}{w_i - w_0 + \Omega} e^{i \Omega t} \right) \quad (\text{S22b})$$

$$= e^{-i w_0(t-t_0)} \mathbf{d}_{i0} \cdot \mathbf{E} \frac{1}{2} \left(\frac{1}{w_1 - w_0 - \Omega} e^{-i \Omega t} + \frac{1}{w_1 - w_0 + \Omega} e^{i \Omega t} \right) \quad (\text{S22c})$$

where t_0 still appears in the overall phase but always cancels in $\langle \mathbf{d} \rangle_t$. In the last line, we have replaced $w_i \rightarrow w_1$ because $\mathbf{d}_{00} = \mathbf{0}$.

The first order part of the dipole moment therefore does not have any static part (the only oscillation frequency is Ω). So, we proceed to the second order, finding

$$a_i^{(2)}(t) \xrightarrow{t_0 \rightarrow -\infty} e^{-i w_0(t-t_0)} \sum_{j=1}^N (\mathbf{d}_{ij} \cdot \mathbf{E})(\mathbf{d}_{j0} \cdot \mathbf{E}) \int \frac{dw}{2\pi} \frac{dw'}{2\pi} \varphi(w) \varphi(w') \frac{1}{w_j - w_0 - w'} \frac{e^{-i(w+w')t}}{w_i - w_0 - w - w'}. \quad (\text{S23})$$

Except for $i = 0$ [which we see from Eq. (S21c) is not needed], we can send the pulse width to zero, yielding:

$$a_i^{(2)}(t) \xrightarrow{\Delta \rightarrow 0^+} e^{-i w_0(t-t_0)} \sum_{j=1}^N (\mathbf{d}_{ij} \cdot \mathbf{E})(\mathbf{d}_{j0} \cdot \mathbf{E}) \left[\frac{1}{4} \left(\frac{1}{w_j - w_0 - \Omega} + \frac{1}{w_j - w_0 + \Omega} \right) \frac{1}{w_i - w_0} + (e^{\pm i 2 \Omega t} \text{ terms}) \right] \quad (\text{S24a})$$

$$= e^{-i w_0(t-t_0)} \sum_{j=1}^N (\mathbf{d}_{ij} \cdot \mathbf{E})(\mathbf{d}_{j0} \cdot \mathbf{E}) \left[\frac{1}{2} \frac{1}{w_1 - w_0 - \Omega} \frac{1}{w_1 - w_0 + \Omega} + (e^{\pm i 2 \Omega t} \text{ terms}) \right]. \quad (\text{S24b})$$

We ignore the $e^{\pm i 2 \Omega t}$ terms because they do not contribute to the static part of the dipole moment at second order.

From Eq. (S21c), we thus obtain the following expression for the static part of the dipole moment at leading order:

$$\begin{aligned} \langle \mathbf{d} \rangle_t^{\text{static}} &= \frac{1}{4} \left[\left(\frac{1}{w_1 - w_0 - \Omega} \right)^2 + \left(\frac{1}{w_1 - w_0 + \Omega} \right)^2 \right] \sum_{i,j=1}^N (\mathbf{d}_{0i} \cdot \mathbf{E}) \mathbf{d}_{ij} (\mathbf{d}_{j0} \cdot \mathbf{E}) \\ &\quad + \frac{1}{w_1 - w_0 - \Omega} \frac{1}{w_1 - w_0 + \Omega} \sum_{i,j=1}^N \text{Re} [\mathbf{d}_{0i} (\mathbf{d}_{ij} \cdot \mathbf{E})(\mathbf{d}_{j0} \cdot \mathbf{E})]. \quad (\text{S25}) \end{aligned}$$

There is a simple interpretation of this expression: the first term is the contribution from the first-order population of the excited states (resulting in a second-order contribution to the dipole moment through $\langle \Psi^{(1)}(t) | \mathbf{d} | \Psi^{(1)}(t) \rangle$), and the second term is the contribution from the second-order population of the excited states, which must be

mediated by a virtual state (which in this model can only be another excited state). We have kept both rotating and counter-rotating contributions.

We may further simplify Eq. (S25) by using a basis for the N degenerate excited states in which the dipole operator is diagonal:

$$\mathbf{d}_{ij} = \mathbf{d}_{ii}\delta_{ij}. \quad (\text{S26})$$

In such a basis, we obtain

$$\begin{aligned} \langle \mathbf{d} \rangle_t^{\text{static}} = \frac{1}{4} \left[\left(\frac{1}{w_1 - w_0 - \Omega} \right)^2 + \left(\frac{1}{w_1 - w_0 + \Omega} \right)^2 \right] \sum_{i=1}^N |\mathbf{d}_{i0} \cdot \mathbf{E}|^2 \mathbf{d}_{ii} \\ + \frac{1}{w_1 - w_0 - \Omega} \frac{1}{w_1 - w_0 + \Omega} \sum_{i=1}^N \text{Re} [\mathbf{d}_{0i} (\mathbf{d}_{ii} \cdot \mathbf{E}) (\mathbf{d}_{i0} \cdot \mathbf{E})]. \quad (\text{S27}) \end{aligned}$$

2. Floquet perturbation theory

We present an alternate calculation of the static dipole moment using the Floquet formalism. We consider the same model as in the previous section, now with the pulse width set to zero from the beginning, i.e.,

$$H^{(1)}(t) = -\mathbf{d} \cdot \mathbf{E} \cos(\Omega t). \quad (\text{S28})$$

The Floquet formalism directly accesses the regime of the broad middle of the wave train in time; in particular, the turning on and off of the pump pulse are not included in this calculation. We consider the start time to be $t = 0$ for convenience.

We now set up Floquet perturbation theory. The Floquet Hamiltonian H_F is an infinite-dimensional, Hermitian matrix defined by

$$(H_F)_{ij,mn} = \frac{1}{\tau} \int_0^\tau dt e^{i(m-n)\Omega t} H_{ij}(t), \quad (\text{S29})$$

where $\tau = 1/\Omega$ is the period and where the Floquet indices m and n go over all integers. With $H(t) = H^{(0)} + H^{(1)}(t)$, we obtain $H_F = H_F^{(0)} + H_F^{(1)}$ with

$$(H_F^{(0)})_{ij,mn} = (w_i - m\Omega) \delta_{ij} \delta_{mn}, \quad (\text{S30a})$$

$$(H_F^{(1)})_{ij,mn} = -\frac{1}{2} \mathbf{d}_{ij} \cdot \mathbf{E} (\delta_{m-n,1} + \delta_{m-n,-1}). \quad (\text{S30b})$$

By Floquet's theorem, there is a complete basis of time-evolving states of the form

$$|\Psi(t)\rangle = e^{-i\epsilon t} |u(t)\rangle, \quad (\text{S31})$$

where ϵ is the quasienergy and where the time-evolving states $|u(t)\rangle$ are τ -periodic. We may write

$$|u(t)\rangle = \sum_{i=0}^N \sum_m e^{-im\Omega t} u_{im} |i\rangle = \sum_\alpha e^{-i\alpha_2 \Omega t} u_\alpha |\alpha_1\rangle, \quad (\text{S32})$$

where $\alpha = (i, m)$ is a two-component index consisting of the level index i and the Floquet index m .

It is convenient to consider an auxiliary Hilbert space spanned by orthogonal basis vectors $|\alpha\rangle$, where we write $|\alpha\rangle$ instead of $|\alpha\rangle$ to avoid confusion with the original Hilbert space. Then we write

$$|u\rangle = \sum_\alpha u_\alpha |\alpha\rangle. \quad (\text{S33})$$

It may be shown that the quasienergies ϵ and the coefficients u_α are determined by an eigenvalue equation with the same structure as the time-independent Schrodinger equation:

$$H_F |u\rangle = \epsilon |u\rangle. \quad (\text{S34})$$

We can thus apply standard time-independent perturbation theory to calculate $\epsilon = \epsilon^{(0)} + \epsilon^{(1)} + \dots$ and $|u\rangle = |u^{(0)}\rangle + |u^{(1)}\rangle + \dots$, yielding the time-dependent wavefunction.

To determine the static dipole moment in the case that the ground state $|0\rangle$ is perturbed by light, we consider the case of $|u^{(0)}\rangle = |0, 0\rangle$ and $\epsilon^{(0)} = w_0$. The static dipole moment is given by

$$\langle \Psi(t) | \mathbf{d} | \Psi(t) \rangle = \sum_{i,i'=0}^N \sum_m u_{(i',m)}^* \mathbf{d}_{i'i} u_{(i,m)} \quad (\text{S35a})$$

$$= 2 \sum_{i=1}^N \text{Re} \left[\mathbf{d}_{0i} u_{(i,0)}^{(1)} \right] + \sum_{i,i'=1}^N \sum_m u_{(i',m)}^{(1)*} \mathbf{d}_{i'i} u_{(i,m)}^{(1)} + 2 \sum_{i=1}^N \text{Re} \left[\mathbf{d}_{0i} u_{(i,0)}^{(2)} \right], \quad (\text{S35b})$$

where, in the second line, we have expanded to second order and recalled $\mathbf{d}_{00} = \mathbf{0}$.

At first order, we readily obtain

$$\epsilon^{(1)} = (0, 0 | H_F^{(1)} | 0, 0) = 0, \quad (\text{S36})$$

and, for $\alpha \neq (0, 0)$,

$$u_{\alpha}^{(1)} = -\frac{(\alpha | H_F^{(1)} | 0, 0)}{\epsilon_{\alpha} - w_0} = \frac{1}{2} \mathbf{d}_{\alpha 0} \cdot \mathbf{E} \begin{cases} \frac{1}{w_1 - w_0 - \Omega} & \alpha_2 = 1, \\ \frac{1}{w_1 - w_0 + \Omega} & \alpha_2 = -1, \\ 0 & \text{otherwise,} \end{cases} \quad (\text{S37})$$

where $\epsilon_{\alpha} = w_{\alpha 1} - \alpha_2 \Omega$ is the unperturbed quasienergy of state $|\alpha\rangle$. The remaining coefficient, $u_{(0,0)}^{(1)}$, can be shown to be pure imaginary (due to the normalization requirement $\langle \Psi(t) | \Psi(t) \rangle = 1$) and represents a phase degree of freedom in the choice of initial state; for convenience, we set $u_{(0,0)}^{(1)} = 0$. Note from Eq. (S35b) that there is no static dipole at first order, since $u_{i0}^{(1)} = 0$ for $i = 1, \dots, N$.

At second order, we obtain

$$\epsilon^{(2)} = - \sum_{\alpha \neq (0,0)} \frac{|\langle \alpha | H_F^{(1)} | 0, 0 \rangle|^2}{\epsilon_{\alpha} - w_0} = -\frac{1}{4} \left(\frac{1}{w_1 - w_0 - \Omega} + \frac{1}{w_1 - w_0 + \Omega} \right) \sum_{i=1}^N |\mathbf{d}_{i0} \cdot \mathbf{E}|^2, \quad (\text{S38})$$

and, for $i = 1, \dots, N$,

$$u_{(i,0)}^{(2)} = \frac{1}{w_1 - w_0} \sum_{\alpha \neq (0,0)} \frac{(i, 0 | H_F^{(1)} | \alpha) (\alpha | H_F^{(1)} | 0, 0)}{\epsilon_{\alpha} - w_0} = \frac{1}{2} \frac{1}{w_1 - w_0 - \Omega} \frac{1}{w_1 - w_0 + \Omega} \sum_{j=1}^N (\mathbf{d}_{ij} \cdot \mathbf{E})(\mathbf{d}_{j0} \cdot \mathbf{E}). \quad (\text{S39})$$

Eq. (S35b) then recovers Eq. (S25). The second term on the right-hand side of Eq. (S35b) is the contribution of the first-order hybridization between $|0, 0\rangle$ and either $|i, 1\rangle$ or $|i, -1\rangle$, while the third term is the contribution from the second-order hybridization between $|0, 0\rangle$ and $|i, 0\rangle$ mediated by either $|j, 1\rangle$ or $|j, -1\rangle$ (both possibilities being summed, in addition to summing $i, j = 1, \dots, N$).

From Eqs. (S31) and (S32), we can also confirm that Floquet perturbation theory recovers the same time-dependent wavefunction as calculated in the previous section (in the limit of $t_0 \rightarrow -\infty$ followed by $\Delta \rightarrow 0^+$) except for the following two features. First, the second-order correction to the quasienergy, $\epsilon^{(2)}$, did not appear in the previous section; however, in the second-order expansion of $|\Psi(t)\rangle$, $\epsilon^{(2)}$ can only appear as a (time-diverging) term in the coefficient $a_{0,I}^{(2)}$ that we did not need to calculate. Second, there is an unimportant overall phase of $e^{-i w_0 t_0}$ between the two calculations, which arises from changing the switch-on time from t_0 to 0.

If we wish to make the approximation of dropping the counter-rotating terms, we can do this directly by setting $\Omega \approx E_1 - E_0$ in Eq. (S25). Alternatively, we can truncate the Floquet Hamiltonian from the beginning so that it acts on the basis states $|0, 0\rangle, |i, 1\rangle$, and $|i, 0\rangle$ ($i = 1, \dots, N$). Then, the static dipole moment consists of a contribution from the first-order hybridization between $|0, 0\rangle$ and $|i, 1\rangle$, and a contribution from the second-order hybridization between $|0, 0\rangle$ and $|i, 0\rangle$ mediated by $|j, 1\rangle$.

3. Equivalence to single-electron approach

As an alternative to the calculations we presented above, that considered the multielectron states directly, we can instead work with single-electron states. Note that, due to strong on-site Coulomb interaction, we can work with spinless electrons. However, it seems that we must neglect the splitting between the ${}^4T_{1g}$ states and ${}^4T_{2g}$ states, because this is a more complicated interaction effect.

In the single-electron approach, we consider

$$H^{(0)} = \sum_a w_a c_a^\dagger c_a, \quad (\text{S40})$$

where the index a goes over five orthonormal, single-electron states: the three t_{2g} states (which we label as g_1, g_2, g_3) and the two e_g states (e_1, e_2). We are interested in the time-evolving dipole moment starting from the following three-electron state:

$$|\Psi\rangle = c_{g_3}^\dagger c_{g_2}^\dagger c_{g_1}^\dagger |\Omega\rangle, \quad (\text{S41})$$

where $|\Omega\rangle$ is the empty state (annihilated by all c_a). The state $|\Psi\rangle$ is the same as the ground state $|0\rangle = |g\rangle$ considered earlier.

The coupling to the pump field is as before. Now we note that the dipole operator is quadratic in the single-electron fields:

$$\mathbf{d} = \sum_{a,a'} c_{a'}^\dagger \mathbf{d}_{a'a} c_a^\dagger. \quad (\text{S42})$$

It is then straightforward to show that the time-evolving dipole moment is the sum of time-evolving dipole moments in the three single-electron states in $|\Psi\rangle$. That is,

$$\langle \Psi | U^\dagger(t, t_0) \mathbf{d} U(t, t_0) | \Psi \rangle = \sum_{a_0=g_1, g_2, g_3} \langle \Omega | c_{a_0} U^\dagger(t, t_0) \mathbf{d} U(t, t_0) c_{a_0}^\dagger | \Omega \rangle. \quad (\text{S43})$$

We can show Eq. (S43) by, e.g., using the time-dependent creation operators. In particular, we may define

$$c_a^\dagger(t) = U^\dagger(t, t_0) c_a^\dagger U(t, t_0), \quad (\text{S44})$$

where we note that the time evolution is in the opposite sense compared to the Heisenberg picture. We then have

$$U(t, t_0) |\Psi\rangle = c_{g_3}^\dagger(t) c_{g_2}^\dagger(t) c_{g_1}^\dagger(t) |\Omega\rangle. \quad (\text{S45})$$

Noting that the canonical anticommutation relation holds at all time ($\{c_a(t), c_{a'}^\dagger(t)\} = \delta_{aa'}$), and noting that the dipole operator is quadratic, we then obtain

$$\langle \Psi | U^\dagger(t, t_0) \mathbf{d} U(t, t_0) | \Psi \rangle = \sum_{a_0=g_1, g_2, g_3} \sum_{a,a'} \{c_{a_0}(t), c_{a'}^\dagger\} \mathbf{d}_{a'a} \{c_a, c_{a_0}^\dagger(t)\}, \quad (\text{S46})$$

which is equivalent to Eq. (S43).

Thus, an alternate approach to calculating the dipole moment is to add up the dipole moments in the three single-electron problems corresponding to the three t_{2g} states.